



NTNU – Trondheim
Norwegian University of
Science and Technology

On the Effect of A to B Stoichiometry Variation on Conductivity and Phase Purity in $0.8\text{BiFeO}_3\text{-}0.2\text{Bi}_{0.5}\text{K}_{0.5}\text{TiO}_3$

Development of Lead-Free Ferroelectric
Materials

Mads Jonas Christensen

Materials Science and Engineering

Submission date: June 2014

Supervisor: Tor Grande, IMTE

Co-supervisor: Maxim Morozov, IMTE

Norwegian University of Science and Technology
Department of Materials Science and Engineering

Acknowledgments

I would like to start by thanking my supervisor, Tor Grande, for the opportunity of working with this exiting project, as well as for the advice and motivation he supplied along the way. Further, I would like to thank my co supervisors Espen Wefring and Maxim Morozov for the many discussions and practical advice. This applies in particular to Espen during the start of the project work, when he used many hours helping me at the lab.

Another thanks goes out to all of the technical staff at the KII building. Jools has many times given me in-depth answers to advanced, and sometimes pointless, questions, as well as given thorough introductions to XRD and SEM. Gunn Torill Wikdahl and Eli-Beate Larsen have both gone out of their way to supply me with equipment and consumables.

I would further like to thank the people of the “ferro group” for our weekly meetings filled with both interesting presentations and discussions, and sometimes also pointless, albeit funny, derailments. The people frequenting 011 also deserve mentioning, for their motivation and presence during tiresome sessions at the lab.

Finally, I would like to give a huge thanks to Guro Heintz and Jørgen Iversen for their companionship and good times at the study room, and for their invaluable proofreading of my report.

Preface

The work described in this report is a continuation of the *project work*¹ conducted fall 2013.[1] This was titled “Investigation of the effect of A-B stoichiometry variation on conductivity in $0.2Bi_{0.5}K_{0.5}TiO_3 - 0.8BiFeO_3$ ”. The results obtained then were not sufficiently convincing, motivating the synthesis and characterization of another batch of samples. Throughout this report, focus is on the new batch, but in some cases, new pellets were prepared from the old samples, and characterized as part of this work. In those cases, the samples are labeled “old batch”. In addition to this, results from the old batch will also be used as a basis for discussion.

Throughout this report, the same color gradient is used when comparing compositions; Excess A samples will always be blue, while A deficient samples will be red.

¹Mandatory research work during the 5th course of Master of Science study programs at NTNU.

Summary

Piezoelectric materials are currently widely used in both electronics and transducer applications. Today, the majority of these units are based on the lead containing material system PZT, and release of lead to the environment during synthesis or through waste is a challenge. Lately, much research has been done into alternative lead-free materials. One of the promising alternatives is bismuth ferrite, $BiFeO_3$ (BFO), which shows high polarization, Curie temperature and strain response, as well as being multiferroic at room temperature. However, the properties are not easily utilized due to high conductivity, yielding leakage currents when external fields in the order of the coercive field are applied.

The too high conductivity appear to originate from p-type conduction, with localized holes, or polarons, on the iron sub lattice. Iron is able to contain several valence states, where Fe^{3+} is default in BFO. Oxidation to Fe^{4+} corresponds to a hole on the iron site, yielding p-type conduction, while reduction to Fe^{2+} corresponds to an electron, yielding n-type conduction. The origin of the intrinsic concentration of holes is argued to be evaporation of bismuth oxide during synthesis, causing bismuth and oxygen vacancies. Oxygen vacancies will then create an equilibrium with holes, in accordance with $2Fe_{Fe}^x + V_O^{\bullet\bullet} + \frac{1}{2}O_O(g) \rightleftharpoons 2Fe_{Fe}^{\bullet} + O_O^x$. Le Chatelier's principle then states that an increase of oxygen vacancy concentration should also cause an increase in concentration of holes, yielding an increase in conductivity.

Synthesis of phase pure samples of BFO has also proven to be a challenge. Silenite and mullite are commonly observed parasitic secondary phases, and bismuth potassium titanate is here solved in BFO in order to avoid these phases. Potassium and titanium stabilize the perovskittic phase, and synthesis of 0.8BFO-0.2BKT (BKTF-80) does not show the same parasitic decomposition. The promising features of BFO are not strongly affected by this composition change, however.

It is here investigated which effect variation of A to B stoichiometry has on conductivity and phase purity of BKTF-80. To do this, samples are prepared where A cation oxides are (1) added for 1 and 2 % A excess, and (2) removed for 1 and 3 % A deficiency, in addition to (3) the stoichiometric sample. This corresponds to $(Bi_{0.9}K_{0.1})_{1+x}(Fe_{0.8}Ti_{0.2})O_3$, where $x = -0.03, -0.01, 0, 0.01, 0.02$.

It is expected that this will cause B vacancies for A excess, and A vacancies for A deficiency, and that these in both cases are balanced by oxygen vacancies. That is, the concentration of oxygen vacancies will be lowest where A excess corresponds to evaporation, and increase with deviation in either direction. The conductivity

is assumed to follow the same development.

Obtained results show that the perovskite phase is not able to accommodate the variation of A to B stoichiometry, but rather secondary phases are formed. Consequently, the expected conductivity development is not observed. To the contrary, conductivity is shown to be lowest for A deficient samples, increasing as stoichiometry is varied toward A excess. This is argued to originate in part from titanium doping, when excess titanium is solved in the perovskite, as opposed to excess iron, which forms a secondary phase. However, the variation in conductivity is so large that other effects are suspected to also play a part.

Further work primarily constitutes investigation of the influence of atmospheric history, as differences due to variations in reducing conditions may help identify the source of conduction.

Sammendrag

Piezoelektriske materialer har et stort bruksområde innen både elektronikk og elektromekaniske enheter. I dag er majoriteten av disse materialene basert på det blyholdige materialsystemet PZT, og utslipp av bly til miljøet under syntese eller avskaffelse av disse enhetene er en utfordring. For å redusere bruken av bly er det de senere årene gjort mye forskning på blyfrie alternative materialer. Et av de lovende blyfrie materialene er bismutferrat, $BiFeO_3$ (BFO), som viser høy polarisasjon, Curie-temperatur, og elektromekanisk kobling, samt at det er multiferroisk ved romtemperatur. Disse egenskapene blir ikke enkelt utnyttet, dog, grunnet en for høy ledningsevne som blant annet fører til lekkasjestrømmer når felt på nivå med det kraftige koersive feltet påføres eksternt.

Den for høye ledningsevnen ser ut til å stamme fra p-type ledning, der ladningsbærerene er lokaliserte hull på jernnettverket i krystallstrukturen, også kalt polaroner. Jern kan inneha flere valensnivå, og i BFO er standard nivå Fe^{3+} . Oksidasjon til Fe^{4+} tilsvarer da et hull på jernplass og gir p-type ledning, mens reduksjon til Fe^{2+} tilsvarer et elektron og gir n-type ledning. Den intrinsiske konsentrasjonen av hull argumenteres å komme fra fordampning av bismutoksid under syntese, hvilket fører til bismut- og oksigenvakanser. Oksigenvakansene vil da utgjøre en likevekt med hull i følge $2Fe_{Fe}^x + V_O^{\bullet\bullet} + \frac{1}{2}O_O(g) \rightleftharpoons 2Fe_{Fe}^{\bullet} + O_O^x$. I følge Le Chateliers prinsipp må økning av konsentrasjon av oksigenvakanser derfor føre til økning av konsentrasjon av hull, og dermed også ledningsevne.

BFO viser også utfordringer koblet til syntese av faserene prøver. Sillenitt og mullitt er ofte observerte parasittfaser, og for å unngå disse løses bismutkaliumtitanat, $Bi_{0.5}K_{0.5}TiO_3$ (BKT), inn i BFO. Kalium og titan stabiliserer den perovskittiske fasen, og syntese av 0.8BFO-0.2BKT (BKTF-80) er ikke plaget av samme parasittiske dekomponering. BFOs gode egenskaper blir likevel i stor grad beholdt.

I dette arbeidet undersøkes hvilken påvirkning A til B ustøkiometri har på ledningsevnen og faserenheten i BKTF-80. Dette gjøres ved å produsere prøver der A-kation-oksid har blitt (1) tilsatt for 1 og 2 % overskudd, samt (2) fjernet for 1 og 3 % underskudd, ved siden av den (3) støkiometriske prøven. Dette svarer da til $(Bi_{0.9}K_{0.1})_{1+x}(Fe_{0.8}Ti_{0.2})O_3$, der $x = -0.03, -0.01, 0, 0.01, 0.02$.

Det forventes at dette fører til B vakanser for A overskudd, og A vakanser for A underskudd, og at disse i begge tilfeller balanseres av oksigenvakanser. Med andre ord vil konsentrasjonen av oksigenvakanser være lavest der A overskudd er lik avdamping, og øke med avvik i begge retninger. Ledningsevnen antas å følge

samme utvikling.

Resultatene viser at perovskittfasen ikke er i stand til å løse variasjonene av A til B forhold, men istedet skiller ut sekundærfaser i tråd med hva som er i overskudd. På grunn av dette observeres ikke den forventede ledningsevneutviklingen. I stedet viser ledningsevnen seg å være lavest for A fattige prøver, og øker jevnt mot A overskudd. Dette argumenteres å delvis komme fra effektiv titandoping fordi overskudd av titan løses i perovskitten, i motsetning til overskudd av jern. Variasjonen i ledningsevne er dog så stor, at det misstenkes at titandoping alene ikke kan være grunnen.

Videre arbeid er i hovedsak undersøkelse av atmosfærepåvirkningen på ledningsevne, da det kan være med å identifisere den underliggende ledningsmekanismen.

Contents

Acknowledgments	i
Preface	iii
Summary	v
Sammendrag	vii
List of acronyms	x
1. Introduction	1
2. Theory and background	5
2.1. Introduction to piezoelectric materials	5
2.1.1. Piezoelectric materials	5
2.1.2. PZT properties	10
2.2. Point Defect chemistry	12
2.2.1. Kröger-Vink Notation	12
2.2.2. Various defects	13
2.3. The BFO-BKT material system	15
2.3.1. BFO	15
2.3.2. BKT	20
2.3.3. Solid Solution	20
2.4. Hypothesis	23
3. Methods	25
3.1. Synthesis	25
3.2. Characterization	27
4. Results	31
4.1. Phase purity	31
4.2. Synthesis	37
4.3. Dielectric properties	40
5. Discussion	47
5.1. Phase purity and actual stoichiometry	47

5.2. Conductivity	50
5.3. Old batch compared to new batch	54
6. Concluding remarks and further work	57
Bibliography	59
A. Additional figures	63
A.1. Rietveld refinement	63
A.2. Dielectric measurements	65
A.3. Results of old batch	66

List of acronyms

BFO	Bismuth ferrite, $BiFeO_3$
BKT	Bismuth potassium titanate, $Bi_{0.5}K_{0.5}TiO_3$
BKTF-x	Bismuth potassium titanate ferrite, x is at% BFO, $x(BiFeO_3) - (1-x)(Bi_{0.5}K_{0.5}TiO_3)$
BNT	Bismuth sodium titanate, $Bi_{0.5}Na_{0.5}TiO_3$
BT	Barium titanate, $BaTiO_3$
CIP	Cold isostatic press
EDS	Energy dispersive X-ray spectroscopy
KN	Potassium niobate, $KNbO_3$
KNN	Potassium sodium niobate, $K_{1-x}Na_xNbO_3$
PT	Lead titanate, $PbTiO_3$
PZT	Lead zirconate titanate, $PbZr_{1-x}Ti_xO_3$
XRD	X-ray diffraction

1. Introduction

Background Piezoelectric materials are used in many devices such as actuators, medical equipment, generators, gas igniters, electrooptic light valves, sensors, microphones, sonars, high dielectric constant capacitors etc., and are therefore of great technological importance.[2, 3] Lead zirconate titanate ($Pb(Zr_{1-x}Ti_x)O_3$, short PZT) constitutes the majority of current piezoelectric devices, presenting a challenge with respect to the hazard of lead containing devices and synthesis thereof.[2, 3] Use of lead in household and industrial applications is restricted by the EU-directive *Restriction of the use of certain Hazardous Substances* (RoHS), but an exception is made for electronic ceramics (i.e. piezoelectric devices), due to the *technical and scientific impracticability* of avoiding it.[2] Much research have been done on possible lead free piezoelectric alternatives[2–14], and one of the promising materials systems is based on bismuth ferrite ($BiFeO_3$, BFO).[2, 6, 8–12, 14–29]

Bismuth ferrite was first investigated for piezoelectric applications in the 1960's[30, 31], and it has been intensively studied after the discovery of enhanced multiferrocity in thin films in 2003.[32] BFO is simultaneously ferroelectric and antiferromagnetic at room temperature, making it the material closest to coupled electric and magnetic properties to date. Coupling of these properties would be of great technological importance with respect to data storage and computer speed. In addition to multiferrocity, BFO exhibits properties such as a very high Curie temperature ($\sim 825^\circ\text{C}$), high polarization ($90 - 100 \mu\text{C}/\text{cm}^2$), and high strain response.[8–10, 28, 33]

Pure BFO is known to be thermodynamically challenging to synthesize, because it decomposes to the parasitic phases $Bi_{25}FeO_{39}$ and $Bi_2Fe_4O_9$ in the temperature interval of $605 - 817^\circ\text{C}$.[16, 27, 28] One approach to mitigate this problem is to solve species stabilizing the perovskitic phase into the material. With this respect, titanium and potassium have been shown to be effective in yielding phase pure samples when added as bismuth potassium titanate ($Bi_{0.5}K_{0.5}TiO_3$, BKT) in excess of 10 at%.[8]

The material system BKT-BFO (BKTF- $<\text{at}\% \text{ BFO}>$) have also been investigated at other compositions than at the BFO end. BKT is a tetragonal ferroelectric, and as BFO is rhombohedral, and a morphotropic phase boundary with accompanying relaxor like behavior has been found at 75 at% BKT (BKTF-25).[8, 9]

While BFO and BFO based solid solutions exhibit useful properties, and phase

1. Introduction

pure samples are being produced, high conductivity remains a challenge. BFO is described as a leaky dielectric, and electric breakdown inhibits the full utilization of the material.[6, 33] Maso and West showed that the conductivity in Ca doped BFO is p-type, with localized polaron hopping on the iron lattice sites.[21] Iron is multivalent, and may either be reduced to Fe^{2+} or oxidized to Fe^{4+} , yielding n-type or p-type conduction respectively.[34]

The source of Fe^{4+} in BKTF is argued to be bismuth/potassium oxide evaporation, yielding A site and oxygen vacancies. The oxygen vacancies will then be filled by ambient oxygen, oxidizing iron in the process.[28] Evaporation of A site cations with negative effects such as increased conductivity is also known from other material systems such as PZT, BNT ($Bi_{0.5}Na_{0.5}TiO_3$) and KNN ($K_{1-x}Na_xNbO_3$).[2, 3]

The effect of bismuth evaporation and unstoichiometry was addressed in previous project work. However, the results obtained were not sufficiently convincing to conclude on any findings.

Aim of work The goal of this work was to investigate the effect on dielectric (i.e. conductivity and permittivity) properties of A-B unstoichiometry in BFO. Because of the challenges of parasitic decomposition, BKTF-80 was used as the *stoichiometric* composition. The combined A cation of BKTF-80 is $(Bi_{0.9}K_{0.1})^{2.8+}$ and, in addition to the stoichiometric sample, this was both (1) added in 1 at% and 2 at% excess and (2) removed for 1 at% and 3 at% deficiency. Compared to a constant B cation $(Fe_{0.8}Ti_{0.2})^{3.2+}$ stoichiometry of 1. This corresponds to $(Bi_{0.9}K_{0.1})_{1+x}(Fe_{0.8}Ti_{0.2})O_{3-\delta}$, where $x = -0.03, -0.01, 0, 0.01, 0.02$ or $\frac{n_A}{n_B} = 0.97, 0.99, 1, 1.01, 1.02$. Negative x correspond to A deficiency, while positive x correspond to A excess.

Perovskites generally do not allow interstitial ions, and the A-B unstoichiometry must therefore be compensated by vacancies. Because of this a more instructive notation of “excess A” may be “B deficiency” so that neither n_a nor n_B are more than one, yielding $\frac{n_B}{n_A} = \left(\frac{n_A}{n_B}\right)^{-1} = 0.9901, 0.9804$ for A excess samples. All unstoichiometry must also be charge compensated by oxygen vacancies, giving rise to δ in the equation above. For consistency in the report, however, the notation used will be either x as described above, or simply A excess/A deficiency, and the reader is asked to keep in mind that “A excess” in practice means “B (and O) deficient”. Or rather, that “excess A” means “B vacancies”, while “A deficiency” means “A vacancies”.

The effect of the stoichiometry variation was investigated both with respect to dielectric properties and by examining secondary phases in XRD and SEM. Combined phase purity results and dielectric properties were then evaluated, giving quantitative information on the A cation evaporation.

The aim of the project work was in essence the same as that of the current

work. Motivating this work is the wish of obtaining a second set of data which, together with the results of the project work, may yield a good foundation for discussion. In the project work, the same stoichiometries were prepared, with the exception that $x = 0.03$ were prepared in the project work, while $x = 0.02$ were prepared here. The change was done because it was apparent that $x = 0.03$ was not close to real 1:1 stoichiometry. A deficient samples were prepared again, however, because they showed interestingly low conductivities.

2. Theory and background

2.1. Introduction to piezoelectric materials

2.1.1. Piezoelectric materials

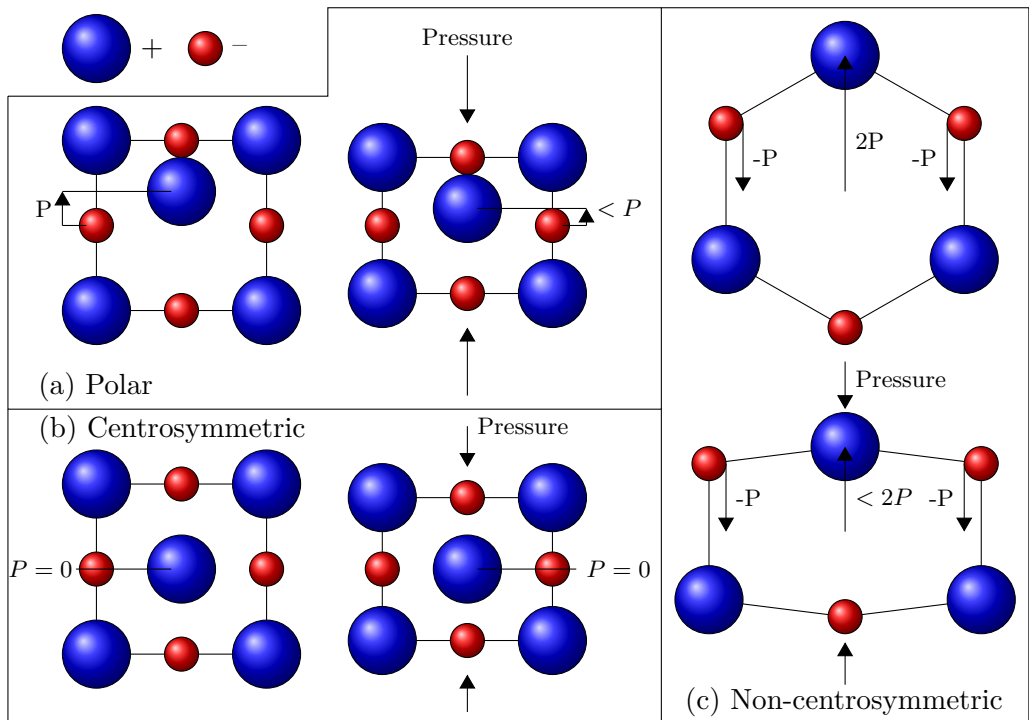


Figure 2.1.: Schematic illustration of the effect of pressure on polarization for different symmetries. (a) Shows that the value of the polarization is changed in spontaneous polar structures. (b) shows that the (absence of) polarization is unaffected in centrosymmetric structures. (c) shows that non-centrosymmetric (unpolar) structures change from net zero polarization to some value different than zero.

Piezoelectric materials are materials that both (1) develop an external voltage when pressed and (2) change dimensions when an external voltage is applied.

2. Theory and background

The word “piezo” originates from Greek, meaning “pressure” or “to press”. Developed voltage as a result of applying pressure is known as “the direct piezoelectric effect”, while dimension change as a result of applied voltage is known as the “inverse piezoelectric effect”. With the piezoelectric effect, polarization is linear with respect to pressure. The related electrostrictive effect¹, however, is weaker and quadratic.

For a material to exhibit piezoelectricity, there has to be some element of non-symmetry in the crystal structure in such a way that deforming of the lattice is associated with a change in electric polarization. More specifically, the point group of the crystal structure has to be non-centrosymmetric, as illustrated in Figure 2.1. The Figure shows which effect pressure has on the polarization in selected structures. Note that the externally available voltage is a result of the sum of the polarizations of the unit cells throughout the material. In the case of permanent polar materials, different effects such as charging of the surface through interactions with air and intrinsic slow conductive mechanisms cause materials left for an extended period of time to appear non-polar. When the internal polarization is changed, however, an external voltage becomes apparent.

Sub-groups There are 32 crystallographic point groups, and 21 of these are, as required, non-centrosymmetric. One of the non-centrosymmetric point groups contains symmetry elements that cancel each other out, leaving 20 piezoelectric point groups. Piezoelectric sub groups are visualized in Figure 2.2.

When the material is spontaneously polarized, it is called a *pyroelectric* material. Ten of the piezoelectric point groups are, in addition to piezoelectric, pyroelectric. The name originates from the fact that as the unit cell parameters of polar materials are changed due to temperature change, the polarization must also change. This is not the case for simple piezoelectric materials, because these have zero net polarization when not under stress. Pyroelectric materials, on the other hand, are spontaneously polarized, and the absolute displacement of the species yielding the polarization is changed along with the unit cell as a whole. As a subgroup, all pyroelectric materials are piezoelectric.

A sub group of the pyroelectrics are the *ferroelectric* materials. These are spontaneously polarized, and this polarization is possible in several directions in the unit cell, allowing switching of the polarization direction. The name is not related to iron, but rather to ferromagnets which show similar behavior with respect to magnetic properties instead of electric.

¹All dielectric materials expand in the direction of an applied field. This is because positive ions will be drawn toward the negative pole, while negative ions will be drawn toward the positive pole. Even purely covalent materials have some degree of “ionicity” because of the difference in electronegativity of the different atoms. Therefore, all insulators of more than one atom type are “dielectrics”, and exhibit electrostriction. Electrostriction will always yield expansion (in the direction of the field).

Ferroelectric materials thus exhibit properties such as hysteresis loops and memory with respect to both polarization and strain. The difference between pyroelectric and ferroelectric materials is not dependent on the point group and cannot be predicted as such.

As ferroelectric materials are heated above a certain temperature, the increased thermal vibrations cause the off-center ions to, on average, be situated in the center, removing the polarization. This temperature is known as the *Curie temperature*, T_C , and all ferroelectric materials are non-polar *paraelectric* above the Curie temperature. At T_C the ions are more easily displaced, hence properties such as permittivity and electromechanical coupling peaks at this temperature. Above T_C , an external field may induce a ferroelectric phase transition.

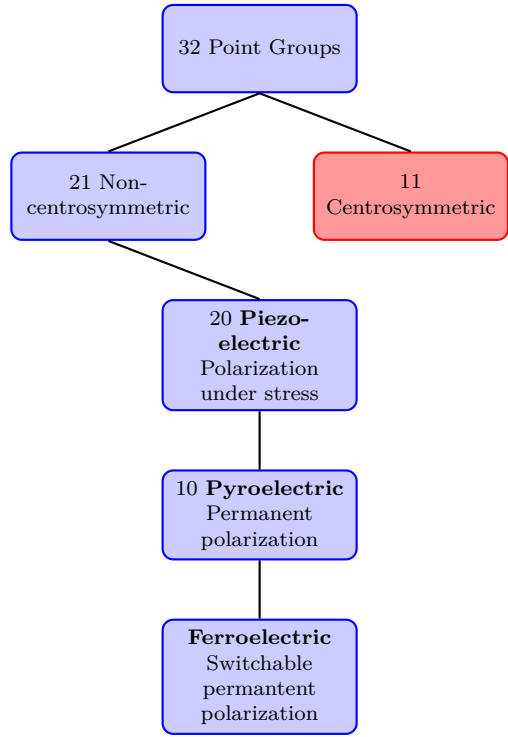


Figure 2.2.: Piezoelectric sub groups.

Piezoelectricity in ceramics The piezoelectric effect illustrated in Figure 2.1 shows that the direction of the polarization, and therefore also the voltage, is dependent on the direction of the grain. In fact, the volume of uniform polarization direction is often different than the size of the grain, and is called a *domain*. As materials are cooled after synthesis, many domains of different orientations are formed. This means that in polycrystalline ceramics where there are many small domains with random orientations, the piezoelectric effect of the different domains will be in different directions and on the whole cancel each other out. Consequently, it was long believed that ceramic materials could never be used for piezoelectric applications. This is not true, however, due to the process known as *poling*.

Poling is done by heating the material above the Curie temperature, applying an external electric field forcing an internal polarization, and then cooling while keeping the field, freezing in the polarization direction. All of the domains will then be directed more or less in the same direction, allowing utilization of the piezoelectric effect. This approach is possible only with ferroelectric materials, leading to an interchangeable use of the the two terms ferroelectric ceramics and piezoelectric ceramics.

2. Theory and background

Common structures Some noteworthy structures exhibiting ferroelectricity are Tungsten Bronze $PbNb_2O_6$, pyrochlore $Cd_2Nb_2O_7$, bismuth layer structure $Bi_4Ti_3O_{12}$, and perovskites ABO_3 . Of these, perovskites are definitely the technologically and educationally most important. Not only is the structure easily visualized and well understood, but it is also thoroughly studied.[2, 3] In addition to this, the historically important $BaTiO_3$ and the commercially important PZT, along with many other ferroelectrics, are perovskites.

Perovskites The perovskite structure is named after the mineral $CaTiO_3$, which again is named after Russian mineralogist Lev Perovski. ABO_3 is the general chemical formula, where A and B stand for different cations and O stands for oxygen. Oxygen is always in the form of O^{2-} , yielding a total charge of -6. The total valency of the cations must therefore be +6, and this is typically distributed as A^{+2}/B^{+4} (II-IV) or A^{+3}/B^{+3} (III-III). When doping with a cation of charge +1 or +5, these will then be situated at the A site or B site, respectively. This is explained through basic geometric considerations when remembering that cations of high valency typically are smaller in size than cations of low valency (see below).

Figure 2.3(a) shows the basic cubic perovskite, with space group² $Pm\bar{3}m$. The A cations make out a simple cubic lattice, with one ion on each of the eight corners. The B cations are situated in the middle of the cell, and the oxygen anions are placed on the middle of each of the six faces, constructing an *octahedron* around the B cation. A network of BO_6 octahedra where each oxygen is shared by two adjacent octahedra is the result. Each B cation is then 6-fold coordinated, as the octahedra contains 6 vertices. In between the octahedra, there are larger *cuboctahedra* (cubically truncated octahedra), sharing 8 triangular “octahedral” phases with the octahedra, and six square “cubical” phases with adjacent cuboctahedra. Because the cuboctahedra contain 12 vertices, each A cation is 12-fold coordinated. The volume ratio of cuboctahedron to octahedron is 5 to 1 for a perfect perovskite, explaining why smaller cations occupy B sites, while larger cations occupy A sites.

Goldschmidt tolerance factor The Goldschmidt tolerance factor relates the sizes of the cations to the distortion from the perfect cubic perovskite. When there is a mismatch of sizes with respect to cation and the void, several distortion and tilting mechanisms occur in order to minimize the mismatch. The tolerance factor is a simple geometric evaluation predicting with reasonable accuracy the type of structure, and is given by

$$t = \frac{r_A + r_O}{\sqrt{2}(r_B + r_O)}$$

²A space group is a notation summarizing all symmetry elements of a structure. See [35]

where $t = 1$ corresponds to a ideal cubic perovskite. $t > 1$ is a result of B cations too small in size, which is often accompanied by a shift of the B cation toward one of the oxygen anions. The resultant loss of symmetry leads to a tetragonal structure, typical for $1 < t < 1.065$, as shown in Figure 2.3(b)/(c). Some commonly known tetragonal perovskites are $PbTiO_3$ (PT), $BaTiO_3$ (BT) and $KNbO_3$ (KN).[28] An even larger t causes the perovskite type structure to become unstable, and consequently hexagonal polytype structures form. t is typically larger than one for I-V and II-IV type perovskites.

When t is less than one and the A cation too small, the resultant disorder is typically tilting of the oxygen octahedra, reducing the size of the cuboctahedra. This gives a rhombohedral structure with polarization along the pseudocubic [111] direction. If t becomes even smaller, the crystal systems changes from rhombohedral to orthorhombic. For $t < 0.86$, the $YMnO_3$ hexagonal structure is typically favored over the perovskite structure. Tolerance factor smaller than one is typically observed for II-IV and III-III perovskites.[28]

In addition to ion size, partly covalent bonds have an important effect on the symmetry of the perovskite, and may stabilize distortions not apparent from the tolerance factor alone. This is seen by tetragonal stabilization of $PbTiO_3$ and $BaTiO_3$ due to partly covalent bonding between empty d orbitals of B cation Ti^{4+} and O^{2-} 2p orbitals.[28] In the case of PT, this stabilization is significantly stronger, apparent by the higher Curie temperature, higher distortion, and stronger polarization. The increased stabilization originates from the important $6s^2$ lone pair of Pb^{2+} which also is partly bonded to O^{2-} 2p orbitals.

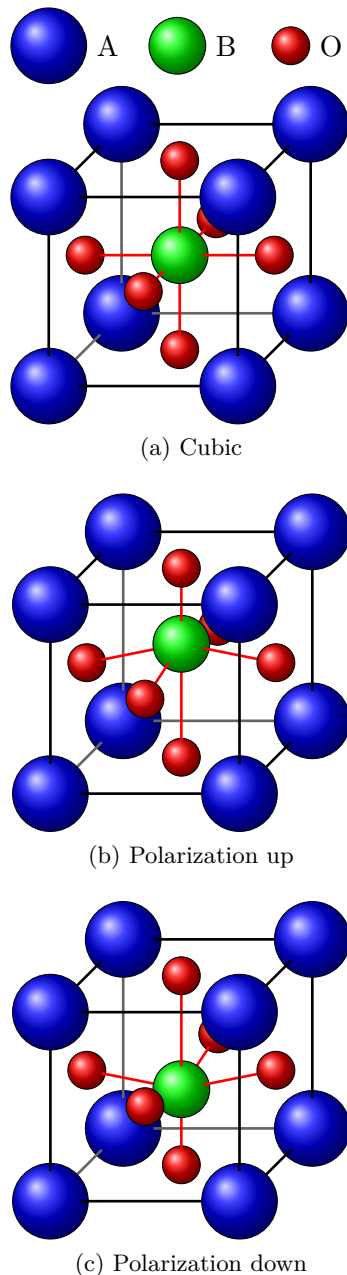


Figure 2.3.: Perovskite structure. Small green B cations are situated in oxygen octahedra, while larger blue A cations are situated in cuboctahedra.

2. Theory and background

Brief history of ferroelectric materials Piezoelectric properties were first discovered in Rochelle salt in 1824, as the relationship between temperature and polarization (i.e. pyroelectricity) was identified. In 1880 Jaques and Pierre Curie found that applying a pressure to the same material also resulted in polarization change and an external voltage. Several other piezoelectric materials were subsequently identified the same year. Following knowledge of ferromagnetic materials, ferroelectric properties were then suggested in 1912, and discovered in Rochelle salt in 1921. Due to structural requirements described above, piezoelectric properties were long expected impossible in ceramics, but *poling* was identified in the the prototype ferroelectric ceramic $BaTiO_3$ in the 1940s. After this, several piezoelectric ceramics have been investigated, leading to a large number of known materials. The most important of this is PZT, which is currently widely used in a number of applications.[3]

Usage The importance of the discovery and development of piezoelectric materials is evident, as possible technological applications are many. Some apparent uses are those of transducers (i.e. devices that transform energy from one form to another). The most obvious transducer use is the devices that use the direct piezoelectric effect, where mechanical tension is converted into electrical signals. Some examples are microphones, accelerometers, power supplies, gas igniters and sensors. On the other hand, the inverse piezoelectric effect enable devices like actuators, loud speakers, micropositioners, sonars, ultrasonic motors, valve controllers and pumps.

One less apparent, but significantly noteworthy, segment of piezoelectric devices are those that take advantage of the high electric permittivity of the materials for use in capacitors.[2, 3] Capacitors are an important part of electronic circuit boards, and piezoelectric materials are therefore included in virtually all electronic devices.

2.1.2. PZT properties

Lead zirconate titanate, $PbZr_{1-x}Ti_xO_3$, is currently the most common material for transducer applications. This is due to several good and tunable properties making the material suitable for many applications. Around the morphotropic phase boundary at $x \sim 0.48$, many properties are maximized, including piezoelectric coefficient, permittivity, and coupling factors.[2] The coercive field is around 1 kV/mm and the remnant polarization is about $35 \mu\text{C}/\text{cm}^2$, while the large signal piezoelectric coefficient can reach values as large as 779 pm/V.[2]

Different dopants and substitutions allow for specialized properties. Donors such as Nb^{5+} for Zr^{3+} and La^{3+} for Pb^{2+} , compensated by A site vacancies, help counteract p-type conduction. In addition to reduced conductivity, donors typically enhance domain reorientation giving square hysteresis loops, low coer-

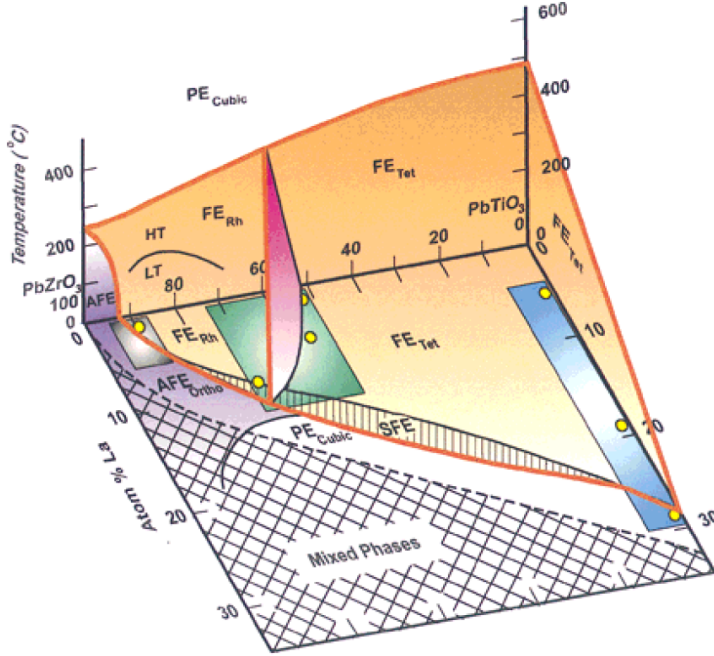


Figure 2.4.: PZT - PLZT phase diagram.[3]

cive fields, high polarization, high dielectric constants, high dielectric loss, high mechanical compliance, and reduced aging. Acceptors such as Fe^{3+} for Zr^{4+} typically has low solubility, are compensated by oxygen vacancies, and generally yield opposite properties as that of donor doping. Other substitutions may influence many of the same properties, as well as Curie temperature, which typically varies from 300 – 400 °C.

The usable temperature range of PZT is up to about 175 °C, above which thermal depoling and increased conductivity becomes a challenge.[2] At typical operating values, 200 V yields a strain of 0.1 – 0.2%. A disadvantage of PZT is its low elastic moduli, comparable to window glass (70 GPa). Typical fracture of PZT is due to low cohesive stress at the crack tip, with intrinsic toughness of 0.7 MPam^{1/2}. In combination with the internal strain differences of different domains after poling, this often becomes the driving force of crack propagation.

One of the most common substitutions in PZT is lanthanum on the lead site, improving a host of properties, including optical transparency.[3] The PLZT phase diagram is shown in Figure 2.4, demonstrating the versatility of the system. From the phase diagram it can be seen that system includes many crystal structures, from antiferroelectric orthorhombic PZ to a rhombohedral ferroelectric phase via the morphotropic phase boundary to tetragonal PT. Increased lanthanum content lowers T_C above which there is a paraelectric cubic phase. The Curie temperature

2. Theory and background

and the solubility of lanthanum is greater at the titanium side of the diagram.

A challenge of the material is the volatility of lead, causing PbO evaporation during calcination and sintering.[3] For this reason, and the fact that liquid PbO phase sintering yields denser sample, excess lead is often added during synthesis. This is also known to increase resistivity, because oxygen vacancies are not created when A deficiency (from evaporation) is removed.

Lead as an environmental challenge The significant use of PZT in piezoelectric applications has led to a significant release of lead into the environment. Both as a result of evaporation and loss during manufacture, but also as waste when piezoelectric devices are discarded. Use of lead in household and industrial applications has been restricted since 2003 by the EU-directive *Restriction of the use of certain Hazardous Substances* (RoHS), due to the known negative effects on living organisms and humans. A temporary exception has been made for PZT in electronic ceramics, however, because of to the *technical and scientific impracticability* of avoiding it.[2] This legislature gave boost to the search for lead-free alternatives, which now constitutes one of the main ceramic technology research areas.[2]

2.2. Point Defect chemistry

2.2.1. Kröger-Vink Notation

Kröger-Vink notation, proposed by F. A. Kröger and H.J. Vink, is a modified chemical reaction notation used to describe point defect chemistry. Compared to regular reaction equilibrium notation, some additional features are introduced. The syntax for species is:

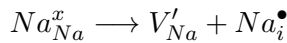
$$Specie_{Lattice\ position}^{Relative\ charge}$$

where the specie could also be a vacancy, V , the lattice position can be interstitial, i , and the charge is relative to the charge of that lattice site in a perfect crystal. Each ' denote a negative charge, x denotes neutral, and \bullet denotes a positive charge.

In addition to the requirement of mass, charge, and oxidation state balance, Kröger-Vink notation introduces lattice site balance. The amount of lattice sites must be equal on both sides of the reaction arrow, with the exception that any integer number of unit formulas may be added to either side.

Some sample equations are the Frenkel and Schottkey defects in sodium chloride, shown in Figure 2.5.

Frenkel defect:



where Na on a Na lattice site is displaced into an interstitial site, creating a vacancy on the Na site. Here, (1) the amount of Na lattice sites, (2) total relative

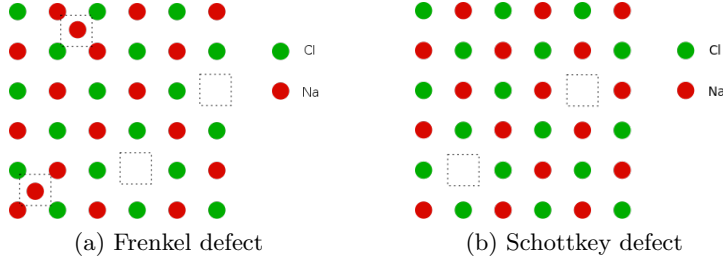
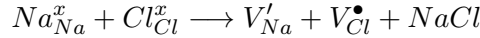


Figure 2.5.: Basic intrinsic defects.[36, 37]

charge, (3) number of ions, and (4) sum of oxidation numbers are the same on both sides. We observe that vacancies and interstitial sites are exempt from balance rules, as vacancies are not mass and interstitial sites are not part of the perfect crystal. A vacancy must be introduced at the right hand side, however, in order to keep balance in Na lattice sites.

Schottkey defect:



where a pair of anion and cation both are removed from the lattice, creating a pair of vacancies. The resulting $NaCl$ can be written as above, or indeed put into a new set of lattice sites, as one whole unit formula of lattice sites is added to the right hand side. In that case, Na_{Na}^x and Cl_{Cl}^x may be removed from both sides, giving the equivalent notation:



2.2.2. Various defects

In addition to vacancies and interstitial atoms/ions, other point defects exist and can be described using Kröger-Vink notation.

Substituted ions are simply written using the syntax previously described. There are three types of substitutions:

Isovalent:

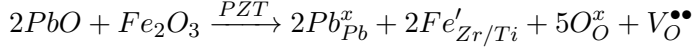


Here Pb^{2+} is replaced by isovalent Ba^{2+} , which can cause effects such as inhibited domain reorientation, changes in phase transition temperatures, and poorly developed hysteresis loops.[3] Notice that the notation above the reaction arrow simply means that the left hand side is introduced to the material noted above the arrow. This defines the available and required lattice sites. In the case of perovskittic PZT, the “perfect crystal” is given by the unit formula $Pb(Zr, Ti)O_3$.

2. Theory and background

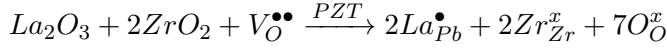
Another example of isovalent substitution is indeed the Zr^{4+} to Ti^{4+} relationship in PZT.

Acceptor doping:



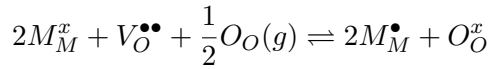
Acceptor doping always produces oxygen vacancies in perovskites because the only charge balancing alternative is interstitial cations, which is rarely observed in perovskites due to the close packed structure. The definition of acceptor doping is that a cation is replaced by another with lower valence. Solubility of acceptor dopants is usually low, and the caused effects are limited domain reorientation, which translates into poorly developed hysteresis loops, lower dielectric constants, low dielectric losses, low compliance and higher aging rates.[3]

Donor doping:

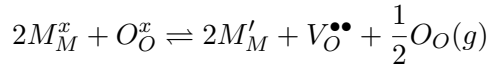


is when a cation is replaced by one of higher valence, here shown for La^{3+} substituting Pb^{2+} . PZT is often donor doped to counteract the p-type conductivity arising from oxygen vacancies. This may decrease the conductivity by at least 3 orders of magnitude in PZT. The combined effects are enhanced domain reorientation, which yields square hysteresis loops, low coercive fields, high remnant polarization, high dielectric constants, maximum coupling factors, higher dielectric loss, high mechanical compliance and reduced aging.[3]

Holes and electrons When the material contains ions capable of several valence states, oxygen vacancies will be in equilibrium with atmospheric oxygen according to



and



Actual concentration of oxygen vacancies is heavily dependent on thermal and atmospheric history, as the equilibria is determined by oxygen partial pressure and temperature, and because kinetics of oxygen diffusion is determined by temperature (and structure).

The off valent metallic ions can then be expressed as as normal ions, but with an electron or hole instead:

$$M_M' = M_M^x + e'$$

or

$$M_M^{\bullet} = M_M^x + h^{\bullet}$$

Resultant conductivity is then given by the Nernst Einstein equation:

$$\sigma = |q|\mu n$$

where q is the charge of the charge carrier, μ is the mobility, and n is the concentration of either holes or electrons. Mobility is relying heavily on band overlapping, in the perovskite structure typically between B cation d orbitals and oxygen 2p orbitals. Generally, early transition metals have larger radii, and therefore a stronger overlapping of orbitals and higher mobility of electrons and holes.

2.3. The BFO-BKT material system

2.3.1. BFO

Crystal structure and ferroic properties Bismuth ferrite is a perovskite with Fe^{3+} B cations in oxygen octahedra and Bi^{3+} A cations in the cuboctahedra. Considering the tolerance factor of BFO, $t = 0.890$ [28], the A cations are too small for the voids. This is compensated by tilting and rotation of the BO_6 octahedra, causing the A cation voids to decrease in size, yielding $\frac{V_A}{V_B} = 4.727$. [28] Both A and B cations is then displaced along the pseudocubic $[111]$ direction, in total giving a rhombohedral distortion of the perovskite. Rhombohedral distortion means that the cubic perovskite has been elongated (or compressed) along the body diagonal of the cube, and the space group of BFO is $R3c$. BFO belongs to the trigonal crystal system, where the unit cell parameters may be expressed in one of three ways; rhombohedral ($a_{rh} = 5.6343 \text{ \AA}$, $\alpha_{rh} = 59.348^\circ$), hexagonal ($a_{hex} = 5.5787 \text{ \AA}$, $c_{hex} = 13.8688 \text{ \AA}$) or pseudocubic ($a_{pc} = 3.965 \text{ \AA}$, $\alpha_{pc} = 89.35^\circ$). [28] Pseudocubic $[111]$ direction is parallel to the hexagonal c axis, which is the notation that will primarily be used in this report. A hexagonal representation of the crystal structure is shown in Figure 2.6.

BFO is ferroelectric, and the polarization direction is along the (hexagonal) c axis, as seen by the upwards shift of both iron and bismuth in Figure 2.6(a). Iron shift inside the octahedra is readily apparent, while the bismuth shift is clear by the fact that bismuth ions are not included in the top (001) plane. Instead, bismuth is shifted above these planes, out of the cell at the top, and into the cell at the bottom. Compared to other ferroelectrics, the polarization, P_S , is stronger than for both $BaTiO_3$ and $PbTiO_3$, and have been measured in thin films, single crystals and cermaic polycrystals at $90 - 100 \mu C/cm^2$. The strength of the polarization is also apparent in Curie temperature, $T_C = 820 - 830^\circ C$, which is very high, as $T_C = 123^\circ C$ and $T_C = 490^\circ C$ for $BaTiO_3$ and $PbTiO_3$, respectively.

Tilting of BO_6 octahedra is important for properties, as the Fe-O-Fe angle controls the overlap of Fe^{3+} 3d and O 2p orbitals. When the angle deviates from 180°

2. Theory and background

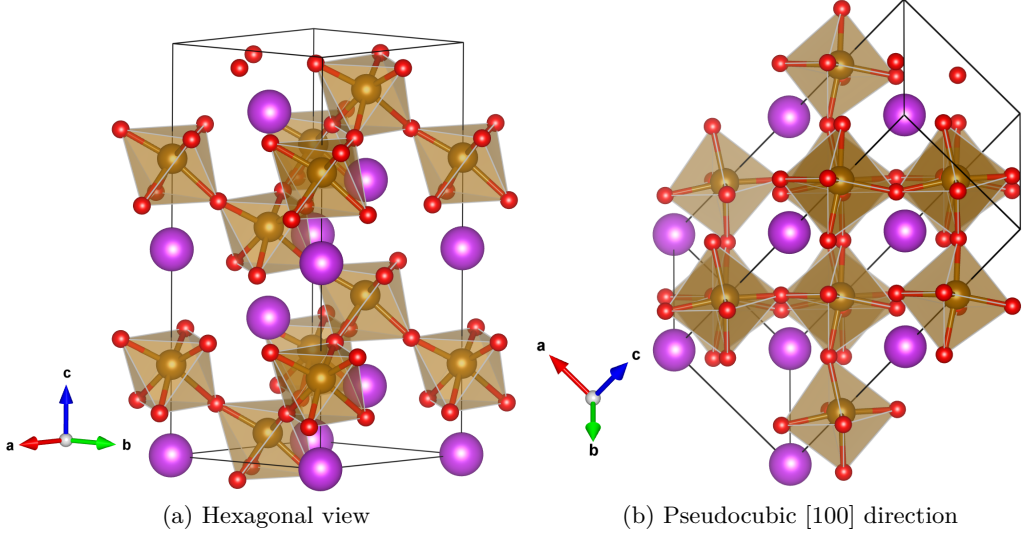


Figure 2.6.: Structure of BFO. Purple spheres: Bi^{3+} . Brown octahedra: $(Fe^{3+}O_6^{2-})$. (a) shows the hexagonal unit cell, while (b) shows the same cell rotated to visualize the tilting of the octahedra. Both subfigures also show ferroelectric displacement of iron inside the octahedra. Lattice sites from [18]. Figure created with Vesta software.[38]

this overlap becomes smaller. For BFO, because of tilting and rotation of octahedra, the Fe-O-Fe angle is $\theta = 154 - 156^\circ$. [16] In octahedral coordination, $Fe^{3+} d^5$ is high spin with localized d electrons, and spectroscopically measured band gap values varies from 2.2 to 2.8 eV. The angle and overlap are also determining the magnetic order.[28]

If BFO had contained only ionic bonding, it would have been centrosymmetric, but, as with PZT, the $6s^2$ lone pair of Bi plays a significant role in stabilization. Computational studies show that there are partly covalent bonding between the Bi $6s^2$ lone pair and O $2p$, which strongly stabilize the displacement of Bi toward the phase of the octahedron in $[001]_{hex}$ direction.[28]

Because of the strong polar displacement, leading to high polarization and T_C , the dielectric constant and piezoelectricity is correspondingly small, at $\epsilon_0 = 30$ and $D_{33} = 15 - 60$ pm/V, respectively.[28] The Neel temperature³, below which BFO is canted G-type antiferromagnetic, is $T_N = 370^\circ\text{C}$.

³The Neel temperature is the magnetic counterpart to the Curie temperature. Magnetic materials are paraelectric above the Neel temperature.

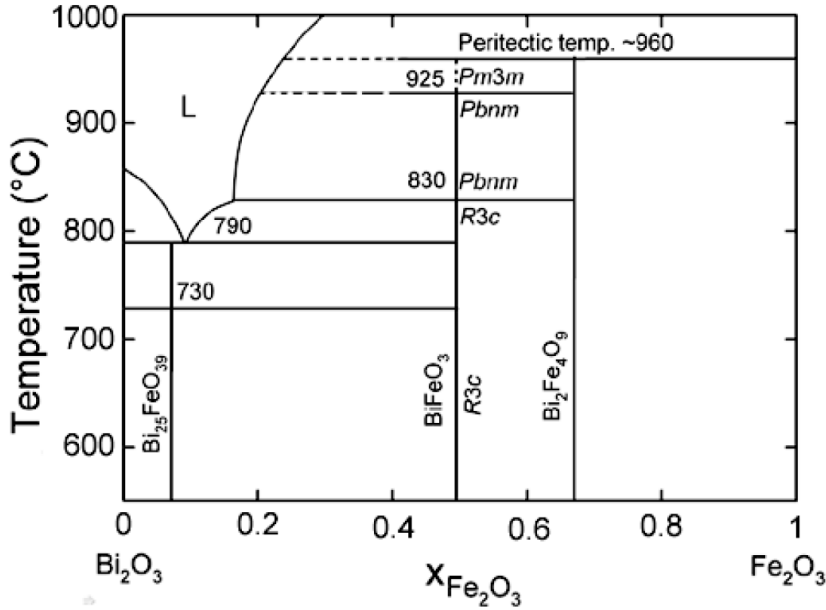


Figure 2.7.: BFO phase diagram adapted from [28].

Thermodynamic stability and synthesis A phase diagram of the binary system $\text{Bi}_2\text{O}_3 - \text{Fe}_2\text{O}_3$ is shown in Figure 2.7. Beside BiFeO_3 and the two binary oxides, two solid phases exist, namely sillenite $\text{Bi}_{25}\text{FeO}_{39}$ and mullite $\text{Bi}_2\text{Fe}_4\text{O}_9$. For all temperatures in synthesis range (i.e. above $\sim 600^{\circ}\text{C}$ where kinetics are fast), deviations from 1:1 Bi:Fe stoichiometry should lead to formation of sillenite or mullite, rather than the binary oxides. This is true until the eutectic melting temperature at 790°C for sillenite, above which a liquid phase forms. At the peritectic temperature $\sim 960^{\circ}\text{C}$ BFO decomposes to a mixture of a liquid bismuth rich phase and iron oxide.

Sillenite and mullite are known as *parasitic* phases and Selbach found that these are thermodynamically stable in the temperature range $605 - 817^{\circ}\text{C}$ [27, 28], causing decomposition of BFO during heating, cooling and holding in this range. Calcination and sintering should thus be executed at temperatures above 817°C , and heating and cooling rates high. Empirically, Selbach found that minimum 825°C for 8 hours with heating and cooling rates of 400°C/h gave phase pure samples within XRD detection limits. [27] Other reported synthesis methods include using 100% excess Bi_2O_3 to avoid $\text{Bi}_2\text{Fe}_4\text{O}_9$, and then leach with diluted HNO_3 several times to remove excess $\text{Bi}_{25}\text{FeO}_{39}$. Another method is the *rapid liquid phase sintering* method where the sample is rapidly heated to 880°C , yielding liquid Bi_2O_3 , and holding for 7.5 min.

Soft chemistry methods such as sol gel are advantageous as these give homogeneous cation mixing on the atomic level. Solid state synthesis on the other hand,

2. Theory and background

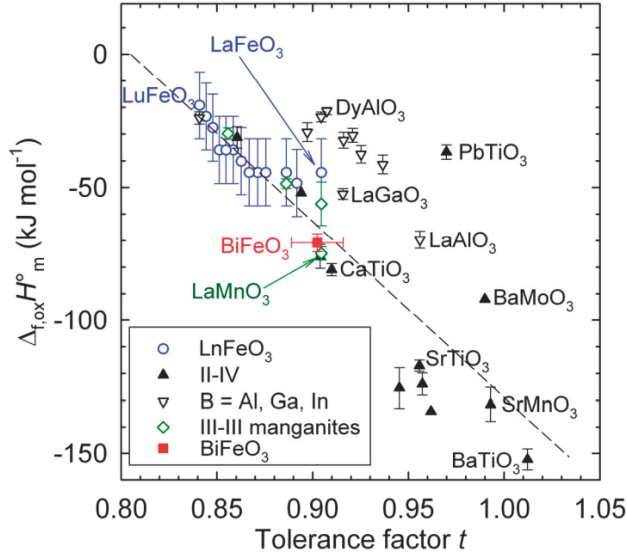


Figure 2.8.: Standard enthalpy of formation for perovskites synthesized from binary oxides vs Goldschmidt tolerance factor. Figure adapted from [28].

requires diffusion in the length scale of the precursor particle size. Because of this, sol gel synthesis require shorter sintering and calcination times, and may be carried out at lower temperatures. Solid state synthesis is, however, generally faster and cheaper than soft chemical methods. For solid state synthesis, acquiring as small particles as possible before calcination is important in order to avoid the need for several sintering and crushing stages, which would increase the impurity levels.

Impurity levels have great influence on the stability of the phases, and thus the phase purity obtained. Frequently used equipment materials, Al_2O_3 and SiO_2 , are more soluble in the parasitic phases, and therefore increase the difficulty of obtaining phase pure BFO. The Gibbs free energy of formation for BFO is close to zero[27, 28], and even small variations in chemical composition can therefore give significantly different phase purity results, even at temperatures well above 817°C. Consequently, reproducibility in BFO is difficult.

Figure 2.8 shows the enthalpy of formation versus tolerance factor for a range of perovskites. On a general basis, a higher tolerance factor is thought to give a more stable perovskite compared to binary oxides. Selbach argues that this might also be transferable to the parasitic phases, and that doping BFO with larger A cations or smaller B cations, increasing t , could lead to increased stability of the perovskite, easing the synthesis process. The acidity of the substitutions is also of importance, and more acidic A cations or more basic B cations are expected to

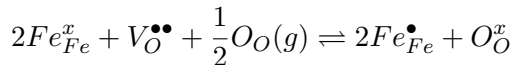
increase the stability of the perovskite phase.

Point defects and conductivity Too high conductivity and leakage currents in BFO is one of the challenges related to the material, and the conductivity mechanism in BFO has been a topic of controversy in literature. Some groups suggest that the charge carriers are holes, or polarons, on the iron sub lattice.[6, 21] In BFO, iron is of valence 3+ [21], but it is well known that both 2+ and 4+ oxidation states may exist. When iron is oxidized to Fe^{4+} , a polaron may “jump” from Fe_{Fe}^{\bullet} via oxygen through Fe 3d and O 2p orbital overlap to another iron. Mobility, μ , is then dependent on the availability/concentration of iron in the sub lattice (reduced for example by substantial substitution of B cations) and by the overlap of orbitals, which again depends on Fe-O-Fe angle and lattice parameters.[16, 28] Concentration of charge carriers, n or p , is simply the extent of iron oxidation, $[Fe_{Fe}^{\bullet}]$.

Other groups, however, argue that BFO is an ion conductor, with oxygen vacancies as the major charge carrier.[21, 23] In this case the conduction mechanism is migration of oxygen vacancies through the lattice. Charge carrier concentration is, of course, simply the concentration of oxygen vacancies, $[V_O^{\bullet\bullet}]$, while mobility is related to the diffusion coefficient of oxygen.

Maso and West combine many of these aspects, and show that Ca doped (acceptor) BFO conductivity is strongly dependent on oxygen partial pressure during heat treatment.[21] As with the typical Brewer diagram, samples treated in oxidizing atmospheres show p-type electronic conduction (Fe_{Fe}'), while samples treated in reducing conditions show oxygen ion conduction. This is in accordance with the equilibrium stated above: $2Fe_{Fe}^x + V_O^{\bullet\bullet} + \frac{1}{2}O_O(g) \rightleftharpoons 2Fe_{Fe}^{\bullet} + O_O^x$. Samples were heavily acceptor doped, and pure BFO can therefore be assumed to be placed closer to the n-type region of the Brewer diagram. In fact, unpublished work by Wefring[34] shows that BKTF-80 do indeed exhibit n-type and p-type conduction after heat treatment in $N_2(g)$ and $O_2(g)$, respectively.

Bismuth is known to be volatile[28], and because of bismuth oxide evaporation during sample preparation, an intrinsic concentration of both bismuth vacancies and oxygen vacancies is present. The oxygen-to-hole concentration is then dependent on partial pressure of oxygen:



Selbach argues that, for the synthesis routes described above, in only a few cases with extra high temperature is evaporation loss of Bi significant. Even powdered samples with high surface area appear to exhibit low Bi pressures when Bi_2O_3 is mixed with Fe_2O_3 .

2. Theory and background

2.3.2. BKT

Bismuth potassium titanate, $Bi_{0.5}K_{0.5}TiO_3$, is in itself a known ferroelectric perovskite. At room temperature the crystal structure is tetragonal, P4mm[9], which changes to a pseudocubic state at $\sim 270^\circ\text{C}$ [39]. This is also the depolarization temperature, which is relatively high.[4] Above this temperature, there are anomalies in the reported piezoelectric properties.[39] The material becomes a cubic paraelectric above the Curie temperature of 380°C [40], which, again, is fairly high compared to for example PZT or $BaTiO_3$. The lattice parameters are $a = 3.913 \text{ \AA}$ and $c = 3.993 \text{ \AA}$. [40]

The ferroelectric properties are promising, but not outstanding. Remnant polarization is $P_r = 22.2 \mu\text{C}/\text{cm}^2$, the coercive field is $E_C = 52.5 \text{ kV}/\text{cm}$, and the piezoelectric constant is $d_{33} = 101 \text{ pC}/\text{N}$. [4, 40]

Synthesis of BKT is challenging particularly due to pores and micro cracks often observed in sintered pellets, which makes the material difficult to pole.[4] Even the densest samples prepared through solid state synthesis is only up to 96% dense. In addition, these samples showed both $K_2Ti_6O_{13}$ and a bismuth rich ternary secondary phases. The artifacts are accredited to evaporation of volatile Bi_2O_3 and K_2O . [40]

Denser samples have been demonstrated through soft chemical methods such as sol gel and hydrothermal sol gel, as well as molten salt synthesis. However, these methods are expensive and complicated. Increased properties for solid state synthesis are reported for samples prepared with an excess of about 1 wt% Bi_2O_3 and KCO_3 . [40] Excess Bi_2O_3 has also been reported to mitigate the problem of micro cracks. [4]

2.3.3. Solid Solution

Solid solutions of bismuth ferrite and bismuth potassium titanate, BKTF-x, where x is at% BFO, have attracted recent attention. (BKTF) At compositions close to 60 at% BFO, Matsuo *et al.* report increased properties in what they argue is a morphotropic phase boundary (MPB). [33] This is similar to PZT, which exhibit a well documented MPB between rhombohedral PZ and tetragonal PTO perovskites. [2, 3, 41, 42] The potential of the BKTF material system for electromechanical applications is supported by Morozov, who report relaxor like behavior for BKTF-25, measuring electric field induced strain values of $250 - 300 \text{ pm}/\text{V}$ in bulk samples. [9] In these cases, the high Curie temperatures of both BFO and BKT is retained, as ferroelectric properties are reported up to 300°C and 175°C , by Matsuo and Morozov, respectively.

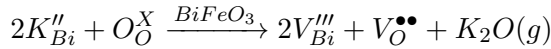
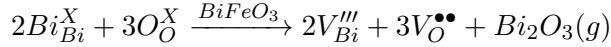
The BKTF material system undergoes several phase transitions with variation of composition. At 100% BFO, the structure is rhombohedrally distorted with symmetry R3c. This symmetry is kept for compositions up to $\sim 40 \text{ at\%}$ BKT,

where there is a phase transition to a pseudocubic phase with polar rhombohedral nano domains. The transition is evident by a $(113)_{R3c}$ peak on BFO side and splitting of the $(111)_c$ peak at BKT side in XRD.[8]. Pure BKT has tetragonal distortion with symmetry P4mm. As the BFO content is increased, splitting of the $(100)_c$ and $(200)_c$ peaks disappear around 25 at% BFO, identifying another phase transition. On the BFO side of this transition, some shoulders remain from the tetragonal BKT splitting, indicating polar nano domains of tetragonal distortion in the BKT end of the pseudocubic phase.

Because BKTF remain rhombohedral up to BKTF-60, BKTF-80 is part of the BFO phase, keeping the ferroelectric and dielectric properties of BFO[8]. Solving BKT in BFO is in this sense a way of stabilizing BFO, as discussed above, and phase pure dense samples are easily prepared by solid state synthesis.[8] The Curie temperature of BKTF-80 is around 670 °C, compared to 820 °C for pure BFO.[1]

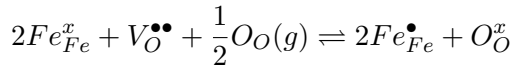
Conductivity As with pure BFO, BKTF-80 is generally too conductive. The material system is complex, and conductivity is not fully understood. It is, however, known that both bismuth and potassium are volatile[8, 28], and from a point defect chemistry point of view, this may explain the origin of charge carriers.

Starting from a stoichiometric sample, A cation evaporation must lead to A vacancies, as B cations are not able to possess interstitial sites in perovskites. In reality, oxide partial pressures are higher than “metallic gas” pressures, and in total it is Bi_2O_3 and/or K_2O that evaporates, creating oxygen vacancies as well. The ratio of bismuth to potassium evaporation is not known. The relevant reactions are:



for bismuth and potassium evaporation, respectively. In both cases, A site and oxygen vacancies are created.⁴ Because of this evaporation, nominal stoichiometric samples are in reality to some extent A deficient.

Increased oxygen vacancy concentration will, because of Le Chatelier’s principle, lead to increased concentration of holes (Fe^{4+}) through:

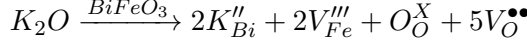
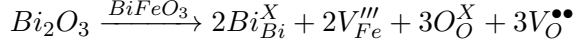


The situation is the same in the case of B-deficient samples. Excess A is not able to possess interstitial sites, and B site vacancies are created. Because of

⁴Note that the A site is labeled Bi^{3+} , rather than $(Bi_{0.9}K_{0.1})^{2.8}$, which is the real “total” A site. This is done for ease and simplicity in notation and because the crystal structure is the same as for pure BFO. Amounts of vacancies, which is the current focus, is not affected by this. Pure BFO is therefore used as reference system.

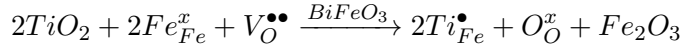
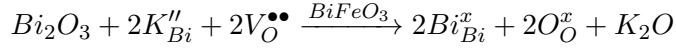
2. Theory and background

charge neutrality, oxygen vacancies must also be created:

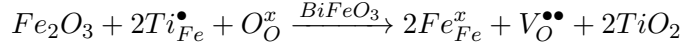
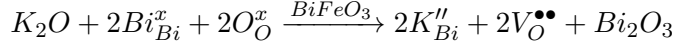


With the same argumentation as above, this should also lead to increased conductivity, assuming that the material is p-type.

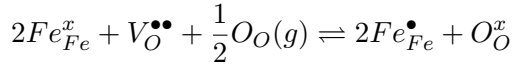
Acceptor or donor doping is also an intrinsic possibility in BKTF because of the different valences of potassium and titanium to bismuth and iron respectively. By shifting the ratio of $Bi^{3+}:K^+$ or $Ti^{4+}:Fe^{3+}$ to the left, ions of higher valence are introduced, yielding donor doping:



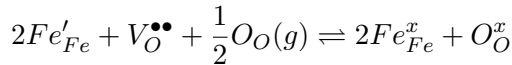
Similarly, shifting to the right yields acceptor doping:



Thus, A to B unstoichiometry or acceptor doping increase the oxygen vacancy concentration, while donor doping decreases it. Assuming polaron hopping as the charge carrier, oxygen vacancy concentration should be as low as possible, shifting



as far to the left as possible, reducing concentration of holes. If, however, the concentration of oxygen vacancies becomes too low, the conductivity will change to n-type, causing increased conductivity with further reduction of vacancy concentration:



In this work, p-type conduction is assumed, and decrease in oxygen vacancy concentration should always lead to decreased conductivity.

In addition to oxygen vacancies and hole concentration, other effect also influence conductivity. Morozov demonstrated the presence of a Maxwell Wagner relaxation barrier (see [12]) shown in Figure 2.9, illustrating one of the complicating factors in conductivity considerations. It is shown that this particular effect is removed by heating the sample to 400 °C, allowing diffusion and reaching of Fe^{4+} equilibrium concentration through the barrier.

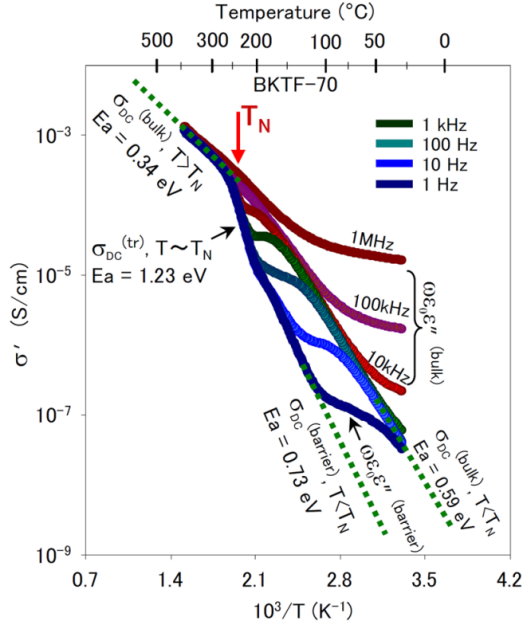


Figure 2.9.: Illustration of Maxwell Wagner relaxation of conductivity present during heating, but not cooling in BKTF-70 samples. Figure adapted from [12].

2.4. Hypothesis

Because nominal stoichiometric samples are A deficient in reality, due to A-cation evaporation, real A:B 1:1 stoichiometry is expected somewhere in the excess A region. Further, the concentration of oxygen vacancies should be lowest at this point, and because of Le Chatelier's principle, also the concentration of holes. That is, a minimum in conductivity is expected somewhere in the excess A region, corresponding to the amount of A cation evaporation. This is visualized in Figure 2.10.

2. Theory and background

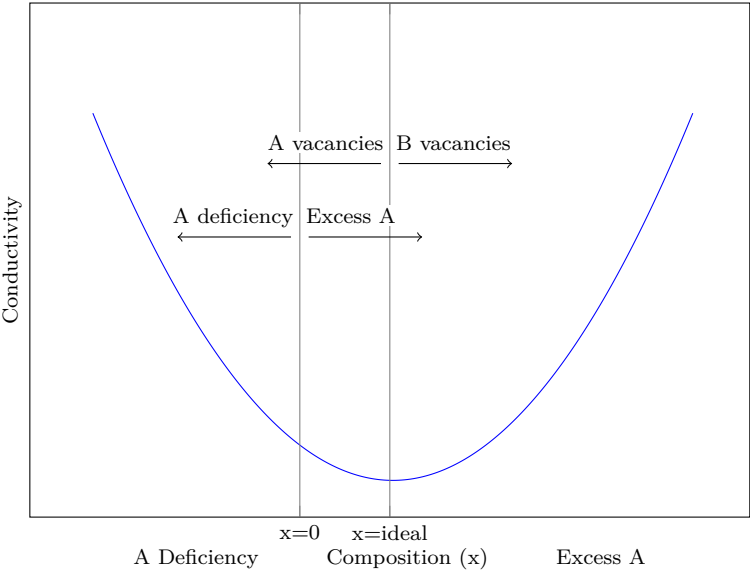


Figure 2.10.: Expected conductivity as a function of composition.

3. Methods

3.1. Synthesis

Samples ranging from 3% A deficiency to 2% excess A were prepared by the solid state synthesis route. Reactant powders (amounts shown in Table 3.1) were carefully weighed before and after drying at 200 °C and 10^{-2} mbar overnight. Weight difference was accredited to water content, and the fraction of water was calculated. Additional reactant powders were then added according to the calculated water content, assuring that the obtained dry powders corresponded to the desired amount of reactants. The reactants used were Bi_2O_3 (99.999%), K_2CO_3 (99.99%), Fe_2O_3 (99.995%) and TiO_2 (99.99%) from Sigma-Aldrich, and the same supply/batches were used for all compositions prepared.

Next, the powders were mixed by wet milling in isopropanol, using 250 ml PE bottles and 470 grams of yttria stabilized zirconia milling balls with a diameter of 5.1 mm. 15 grams of isopropanol for 20 grams of powder gave slurries of decent viscosity. All compositions were milled simultaneously on the same mill for 24 hours at a speed manually adjusted to give a milling ball angle of 60°.

Following milling, the milling balls and bottles were rinsed with isopropanol, and the obtained slurries were dried using a rotary evaporator, with a bath temperature of 46 °C, at 62 mbar. The dry powders were then collected using plastic spatulas.

Calcination was done in alumina crucibles using lids without any gap, in order to try to minimize the loss of A site cations through evaporation. Heating and cooling rates were set at 300 °C/h, but the cooling rates were slower due to the oven only being air cooled. The calcination temperature was 820 °C, and the holding time was 5 hours.

Table 3.1.: Rectant powders target masses in grams.

x	Bi_2O_3	K_2CO_3	Fe_2O_3	TiO_2
−0.03	14.1009	0.4647	4.4284	1.1074
−0.01	14.2026	0.4681	4.3702	1.0928
0	14.2524	0.4697	4.3417	1.0857
0.01	14.3017	0.4713	4.3136	1.0787
0.02	14.3502	0.4729	4.2858	1.0717

3. Methods

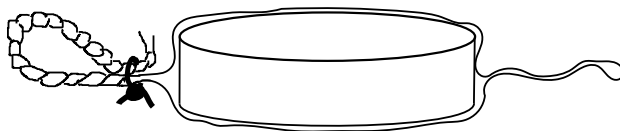


Figure 3.1.: Illustration of pellet wrapped and sealed in latex sample condom for pressing in CIP.

After calcination the powders were once again milled; this time, however, with fewer milling balls in smaller bottles due to the assumed larger particle size after calcination. Using 255 g milling balls and 10 g isopropanol, the powders were milled in 100 ml bottles for another 24 hours. Again, the slurries were rinsed into the rotary evaporator beaker and dried in the same conditions as above. To remove remaining moisture the dried powders were kept at 110 °C overnight before being ground with mortar and pestle, and sieved through a 250 μm mesh stainless steel sieve.

Sintering pellets Pellets were first pressed uniaxially in 10 mm diameter circular stainless steel dies using 56 MPa of force for more than 2 minutes.¹ After uniaxial pressing, the samples were put in several layers of small latex sample condoms which were evacuated of air and sealed by twisting and tying a string around the twist as shown in Figure 3.1. These were further put together in a nitrile glove which also were evacuated and sealed, and isostatically pressed in a cold isostatic press for more than two minutes at 2 kbar.

After pressing, the pellets were put on a bed of sacrificial powder (unpressed powder from the same sample) in alumina crucibles, and covered with more of the same sacrificial powder. Lids were used in the same fashion as during calcination. Weights of pellets, clean crucibles and sacrificial powder were recorded. Sintering was conducted with 120 °C/h heating and cooling rates, and held for 2 hours in unmodified atmosphere and pressure. The sintering temperatures were 1010 °C for stoichiometric and A deficient samples, and 1030 °C for A excess samples.² After sintering, the width of the samples varied from 1.5 to 4 mm.

The same oven and crucibles were used for both calcination and sintering, and when possible, pellets of more than one composition were sintered simultaneously, but in different crucibles. In total, two crucibles were used for calcination, and an additional two were used for sintering. Only BKTF-80 had been prepared in the

¹Pellet weights varied from 0.7 grams to 1.5 grams, where small pellets were used for SEM imaging, and large pellets were used for dielectric measurements and Archimedes' method. Pellets of varying size were combined and ground for XRD.

²These temperatures were adapted from the project work [1], and were originally chosen because secondary phases were detected in excess A samples after sintering at lower temperatures. In the project work, sintering at higher T appeared to yield more phase pure samples.

crucibles prior to this work, and they were simply wiped clean with paper tissues between uses.

Measures to prevent contamination Throughout the experimental work much effort was made to minimize the amount of impurities introduced to the samples. In addition to high purity reactant powders, the equipment used was thoroughly cleaned, and in many of the synthesis steps, dedicated “BKTF-80 equipment” was used. The dedicated equipment includes milling balls and containers, sieve for rinsing the milling slurry, mortar and pestle, sieve for breaking agglomerates before pressing pellets, and even the dish brush used for cleaning the equipment. For calcination and sintering, the alumina crucibles used had also only been used for BKTF-80 in advance.

3.2. Characterization

The main characterization methods applied in this project are scanning electron microscopy imaging (SEM), energy dispersive X-ray spectroscopy (EDS), X-ray diffraction (XRD), and dielectric spectroscopy. In addition, some other measurements such as Archimedes’ method for porosity were used.

SEM Pellets prepared from all samples were investigated in SEM. Back surfaces of the pellets were polished quickly with coarse silicon carbide paper and cleaned before being attached with carbon tape to the same piece of aluminium sheet. The samples were then placed front-side-down in a mold and the aluminium sheet was guided away from the pellets creating a current pathway through the epoxy in which the samples were cast. This gave one sample piece of epoxy containing all samples in the same surface plane. The combined sample was then ground planar with #800 silicon carbide paper, roughly ~ 0.5 mm into the actual samples, assuring that the bulk of the samples was reached. After grinding, the samples were polished using automated sequences on Struers’ Tegramin preparation system with DiaPro diamond suspensions. Plan Dur and Nap, with diamond sizes of $9\text{ }\mu\text{m}$, $3\text{ }\mu\text{m}$ and $1\text{ }\mu\text{m}$, respectively, were used before finishing with the surfactant solution Chem.

For characterization, the Hitachi S-3400N SEM equipped with a Oxford X-max EDS detector was used. Secondary electron and backscattered electron images were obtained using 120 s collecting times at 1280×720 pixels resolution, assuring high signal-to-noise ratio and nice pictures. EDS mapping was conducted in Oxford’s proprietary AZtec software with the TruMap and drift correction functions, with collecting times ranging from 1 – 2 hours for the maps in Figures 4.1 and 4.3. Low accelerating voltage, $V_{Ac} = 10\text{ kV}$, was chosen for increased resolution, and high probe current was set for high X-ray intensity and fast collection.

3. Methods

Imaged, calcined, and milled particles were subtracted from the milling slurry shortly after milling. New plastic spatulas were simply put into the milling ball/slurry mixture, and the attached slurry was rinsed off of the spatula by isopropanol into a sample glass, and further diluted with isopropanol. This mixture was shaken before extracting some of it from the bottom of the sample glass with a pipette. One drop was then added to clean SEM sample stubs and allowed to dry, before being investigated in SEM. The particles on the sample stub were at this point not visible with the naked eye.

XRD For X-ray diffraction, both Bruker D8-Focus, and Bruker D8-DaVinci were used. Both instruments utilize $Cu K_\alpha$ radiation and linear detectors.

Measurements of old samples for refinement in Topas during this work were conducted in the D8-Focus. In these scans, 0.2 mm slit, 90 min collection times, 0.02° step size over the range $2\theta = 20 - 90^\circ$ were used. Due to limited availability of sample powder, smaller cavity silicon sample holders were used.

New samples, both calcined and sintered, were measured in the DaVinci XRD. Calcined powders were measured on single crystal silicon sample holders with 30 min collection times and 6 mm variable slit sizes.

The surfaces of sintered pellets were ground off, and the remaining bulk were crushed and ground using mortar and pestle, yielding ~ 2 g remaining powder for each sample, and then annealed at $700^\circ C$ for 1.5 hours in the same alumina crucibles used for calcination in order to remove ferroelastic strain from the samples. The XRD collections were conducted for 120 min in regular cavity plastic holders with $2\theta = 20 - 80^\circ$ and step size 0.013° .

Rietveld refinement was done in Bruker's software Topas, using the structure and lattice parameters of pure BFO [28] as the starting point for fitting. Correct instrument characteristics were supplied, and the fundamental parameters peak shape option was chosen.

Approach to tackle peak broadening in refinement For old samples, challenges of poor fit due to anisotropic peak broadening were attempted to be avoided by adding a second "helping" phase to the fitting process. This second phase was created as a cubic phase with starting lattice parameters to give peaks at the areas of peak broadening. Then, strain and crystallite size were set to give much peak broadening, so that this phase would cover the broadened parts of the collected data. This approach was implemented with the wish that it would allow the rhombohedral phase to be more freely fitted to the actual peaks. Figure A.1 in the appendix shows the results of two selected peaks from the fitting with the additions from both the helping phase and the rhombohedral phase. Figure A.2 shows the difference of total fit with and without the helping phase. The viability of this approach is briefly discussed in sub chapter 5.1.

Dielectric spectroscopy Dielectric properties were measured with a Probostat instrument from NorECs in a water cooled tube furnace. In the setup, a circular disk sample was placed between two platina electrodes connected to the voltage source by platina wires. Wire-electrode-sample-electrode-wire was pressed together by a spring loaded alumina disk, and all of this was put inside a sealed alumina tube. A controlled atmosphere flow of synthetic air (20% O_2 , 80% N_2) was introduced inside the tube, which was then placed inside the furnace. A thermocouple placed on the other side of a thin alumina disk from the sample measured the temperature. The four wire setup of the Probostat hardware was used, and permittivity and conductivity were measured as a function of temperature and frequency of the applied voltage.

Samples different batches were prepared differently. However, the batches had in common that the sample surfaces were ground planar and parallel with #800 silicon carbide paper. The old samples were then ground with finer #4000 silicon carbide paper, while the new samples were polished lightly with 9 μm and 3 μm diamond suspensions. Old samples were rinsed in water and ethanol, while new samples were washed in ethanol in ultrasonic bath for one hour. The circumference of the pellets was then covered with regular office tape, exposing only the flat surfaces, which were coated in Ar atmosphere in a gold sputterer set to 15 mA current for 15 minutes on both sides. For old samples, the thickness after grinding/polishing was ~ 1 mm, while the new samples had thickness ~ 3.5 mm. All samples had diameters of ~ 8 mm.

The same procedure of measurements was used for both samples from the old batch and from the new. During all heat treatments, dielectric properties were measured every 30 seconds for frequencies 10^0 – 10^6 , one decade step length, independent of the current temperature. Every sample was heated twice after being connected to the instrument. First, 120 $^\circ\text{C}/\text{h}$ heating and cooling rates from room temperature to 400 $^\circ\text{C}$ (no holding time) in order to allow removal of Maxwell Wagner surface effects introduced during gold electrode coating. Maxwell Wagner removal was followed by heating to 700 $^\circ\text{C}$ (no holding time) using the same heating and cooling rates. The latter measurements were finally used for bulk dielectric property considerations.

Before and after each heat treatment step, the samples were measured at room temperature over an extended frequency range to check for any deviations due to for example electrode damage or improper assembly etc.

Archimedes' method Density of the samples was measured by Archimedes' method in isopropanol. First, the sample surfaces were lightly ground to remove excess sacrificial powder, and cleaned with ethanol in ultrasonic bath to remove particles from the open pores. Then, the samples were dried at 110 $^\circ\text{C}$ overnight, and weighed, after which they were held at less than 0.0025 bar for 15 min, before

3. Methods

introducing isopropanol to the chamber. The samples were then held submersed for 30 min to let the open pores fill, before atmospheric pressure was introduced. Temperature stabilization was obtained by waiting another 30 min. Finally, the samples were weighed submersed in isopropanol, and in air after wiping off excess isopropanol with a moist tissue.

Bulk density was then calculated using

$$\rho_b = \frac{m_{dry}}{m_{wet} - m_{sub}} \rho_{liq}$$

where m_{dry} , m_{wet} and m_{sub} are weights of dry, wet and submersed samples, respectively, and ρ_{liq} is the density of isopropanol, given by

$$\rho_{liq} = -0.0009T + 0.8018 \text{ (g/cm}^3\text{)}$$

Total density is then given by

$$\rho = \left[1 - \left(\frac{\rho_t - \rho_b}{\rho_t} \right) \right] \cdot 100\%$$

where the theoretical density, ρ_t , is assumed to follow a linear relationship from the densities of pure BFO and BKT:

$$\rho_t = 0.8 \cdot \rho_{BFO} + 0.2 \cdot \rho_{BKT} = 7.912 \text{ g/cm}^3$$

where $\rho_{BFO} = 8.40 \text{ g/cm}^3$ [28], and $\rho_{BKT} = 5.96 \text{ g/cm}^3$ [34]. Changes in theoretical max weight due to variation in nominal A-B stoichiometry was not taken into account.

4. Results

4.1. Phase purity

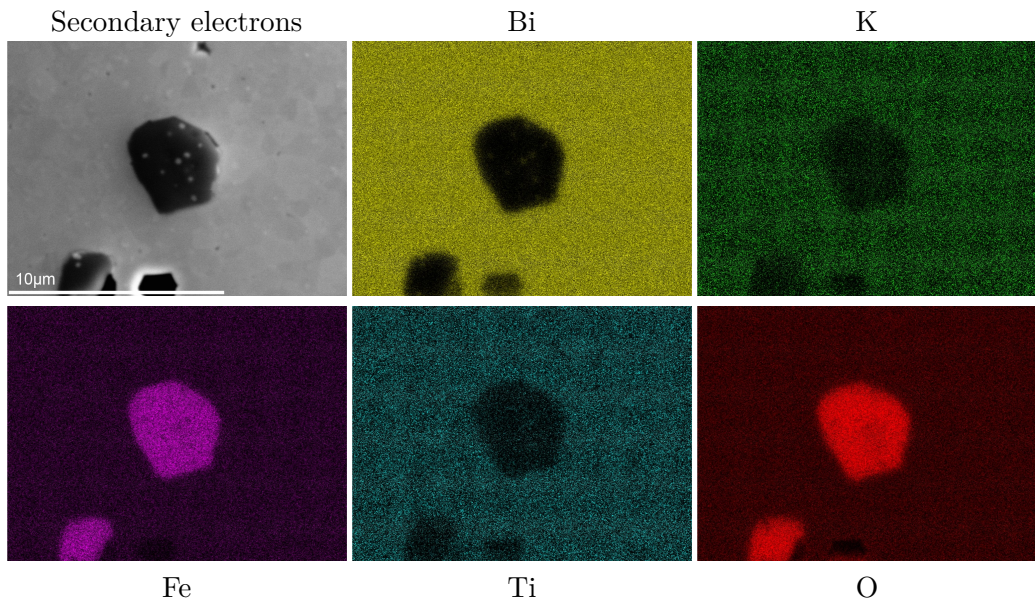


Figure 4.1.: EDS mapping of 3% A deficiency sample showing the distribution of species throughout the the dark secondary phase observed in A deficient samples in Figure 4.2.

SEM Polished samples of all compositions were investigated in SEM, and images are shown in Figure 4.2. When using the secondary electron detector (left column in Figure 4.2), pores are clearly visible in all samples. For A deficient samples and the stoichiometric sample, the pores appear to be of the same size and in the same amount. For excess A samples however, the pores are fewer in number, but significantly larger in size. In addition to pores, stoichiometric and A deficient samples show a dark secondary phase distinguishable from the pores by the lack of an intensity-rich ring (topography contrast) at the border of the dark areas. Secondary electron detectors also detect some backscattered electrons, which is the origin of the observed contrast between the matrix and the secondary phase. In the case of backscattered electron images, this contrast is so strong that it is difficult to

4. Results

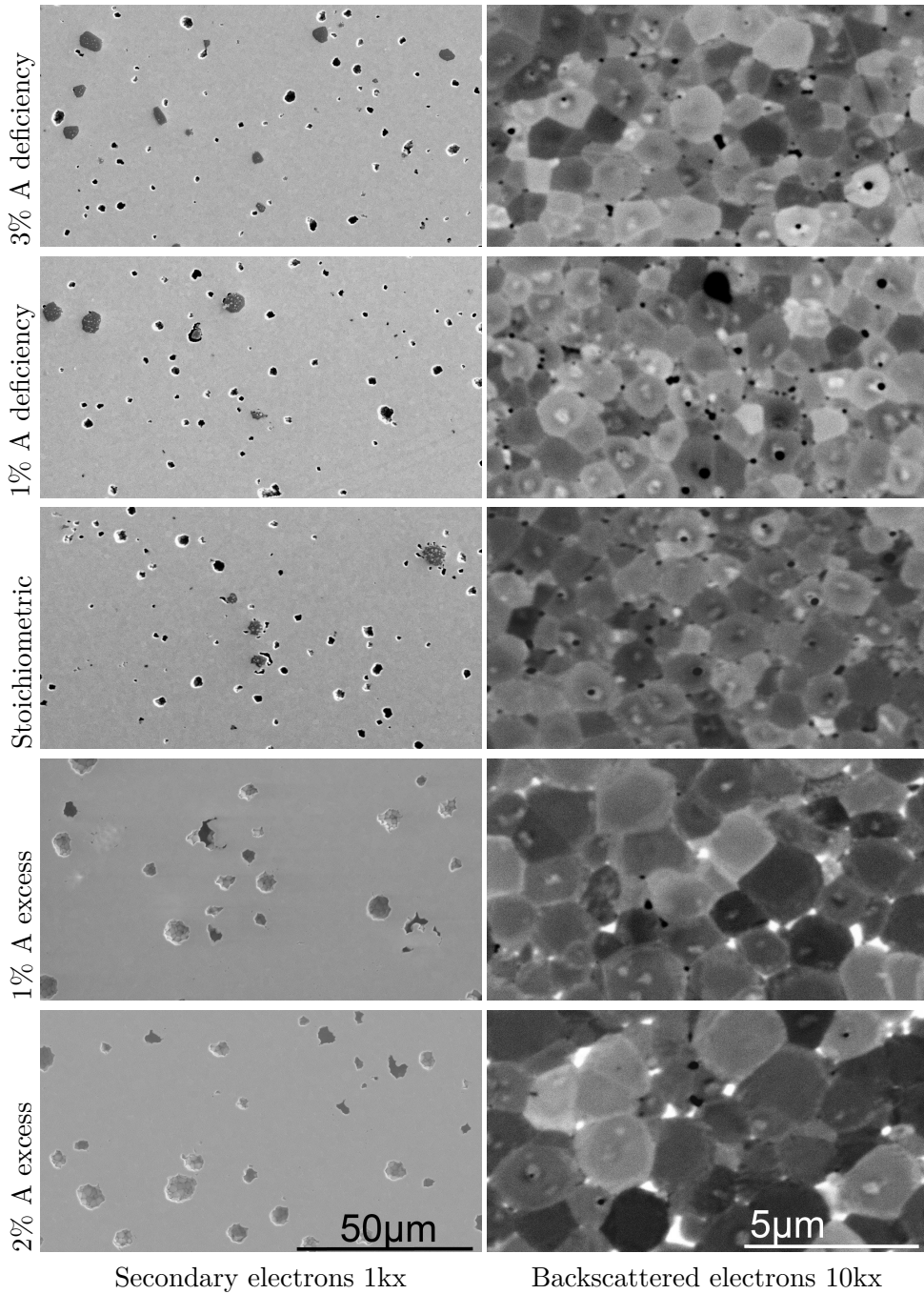


Figure 4.2.: SEM images of ground and polished pellets. Left column shows the development of the content of a dark secondary phase as well as the pore size. Right column shows images taken with very high contrast in order to distinguish individual grains, and the presence of a bright secondary phase. All images in one column are taken with the same SEM conditions.

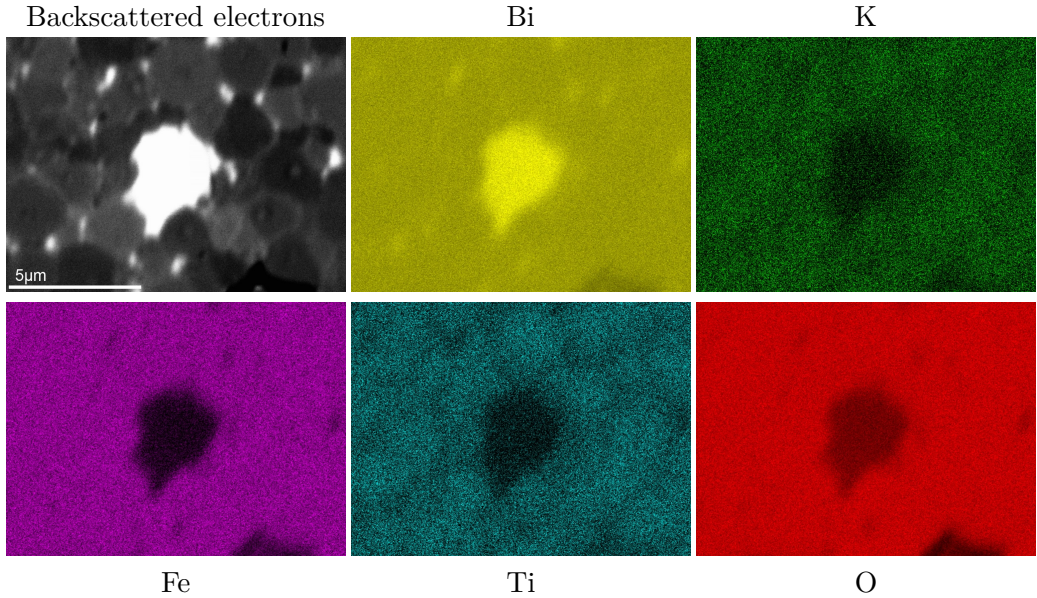


Figure 4.3.: EDS mapping of 3% A excess sample showing the distribution of species throughout the the bright secondary phase observed in Figure 4.2.

distinguish the secondary phase and pores. Consequently, the secondary electron detector was used to take images of the dark secondary phase.

The amount of this phase appears to be increasing with the deviation from stoichiometric composition. Inside the secondary phase areas, small inclusions of the same color as the surrounding matrix can be observed. The diameter of secondary phase areas range from $\sim 1 \mu\text{m}$ to $\sim 10 \mu\text{m}$. In figure 4.1, the phase is shown by EDS mapping to be heavily iron (B-cation) and oxygen rich, while the small dots included in the secondary phase appear to be of the same composition as the matrix. A randomly selected area of the 3% A deficiency sample was used for the mapping. Figure 4.1 also shows some possible segregation of Ti and K cations, but the resolution is too low to be conclusive. Notice also that the iron rich secondary phase does not contain a significant amount of the other B cation, titanium.

Backscattered electron images with higher magnification are shown in the right column of Figure 4.2. The contrast was set very high during the capture of these images in order to distinguish the different grains through orientation contrast. A bright secondary phase is clearly visible in the two excess A samples. The phase is typically situated at the corners between grains, and are in the order of 500 nm wide. An unusually large area of this phase was located (because of the limited resolution power of EDS) and used for EDS mapping, as shown in

4. Results

Figure 4.3. The mapping proves the phase to be bismuth (A cation) rich, in accordance with the high brightness of the phase (increased electron scattering of heavier elements). Because of the increased electron scattering in this bismuth rich phase, the penetration depth of the electrons will be significantly smaller, and the effective volume of X-ray generation will be smaller than that of the matrix. This is manifested in the decreased oxygen X-ray intensity observed in the map, which should be more or less continuous assuming that the phase is bismuth oxide rather than bismuth metal. The same effect should be expected for all element maps, and the chemical composition of this phase is not at all accurately given by EDS mapping.

Segregation of K and Ti is also showing in this map, and appear more distinct than in the secondary electron images due to the higher magnification. From these images, it is clear that the segregation corresponds to the grain boundaries, which appear to be both potassium and titanium poor. It is noted that there is no increased intensity of the other elements on the grain boundaries, however.

Grain size Figure 4.2 shows that the grain size is in the order of $1.5\ \mu\text{m}$ for stoichiometric and A deficient samples, whilst in the order of $2.5\ \mu\text{m}$ for excess A samples. It should be noted that the excess A samples were sintered at $1030\ ^\circ\text{C}$, while the remaining samples were sintered at $1010\ ^\circ\text{C}$. Bismuth oxide is known to have a melting temperature of $824\ ^\circ\text{C}$ [43], and should therefore be liquid during sintering. In the samples with excess A, this liquid phase on the grain boundaries will also have facilitated grain growth.

XRD XRD scans of all compositions are shown in Figure 4.4. From the secondary peak at $\sim 28^\circ$, $x = 0.02$ is shown to contain a secondary phase (marked by o) not present in $-0.03 < x < 0.01$. Matching of secondary peaks identifies this phase as $\text{Bi}_{25}\text{FeO}_{39}$ (ICDD 04-008-8064) or some solid solution variation of Bi_2O_3 . Oppositely, the inset in the figure shows an iron rich secondary phase (v) present only for $-0.03 < x < 0.01$. The reference phase is hematite $\text{Fe}_{1.92}\text{O}_3$ (ICDD 01-077-9924), and the secondary phase may be any solid solution variation of Fe_2O_3 .

These observations are in accordance with both the bright and the dark secondary phases observed in SEM, with the exception of the iron-bismuth secondary phase transition happens in the range $0 < x < 0.01$ for SEM, and $0.01 < x < 0.02$ for XRD.

Note that all samples contain only one secondary phase, and that the parasitic iron rich mullite phase, $\text{Bi}_2\text{Fe}_4\text{O}_9$, known from pure BFO[28] is not present at all in any sample, showing that solving BFO with BKT is effective in remedying the challenges of parasitic decomposition.

Because all samples exhibit some secondary phase however, it seems that either

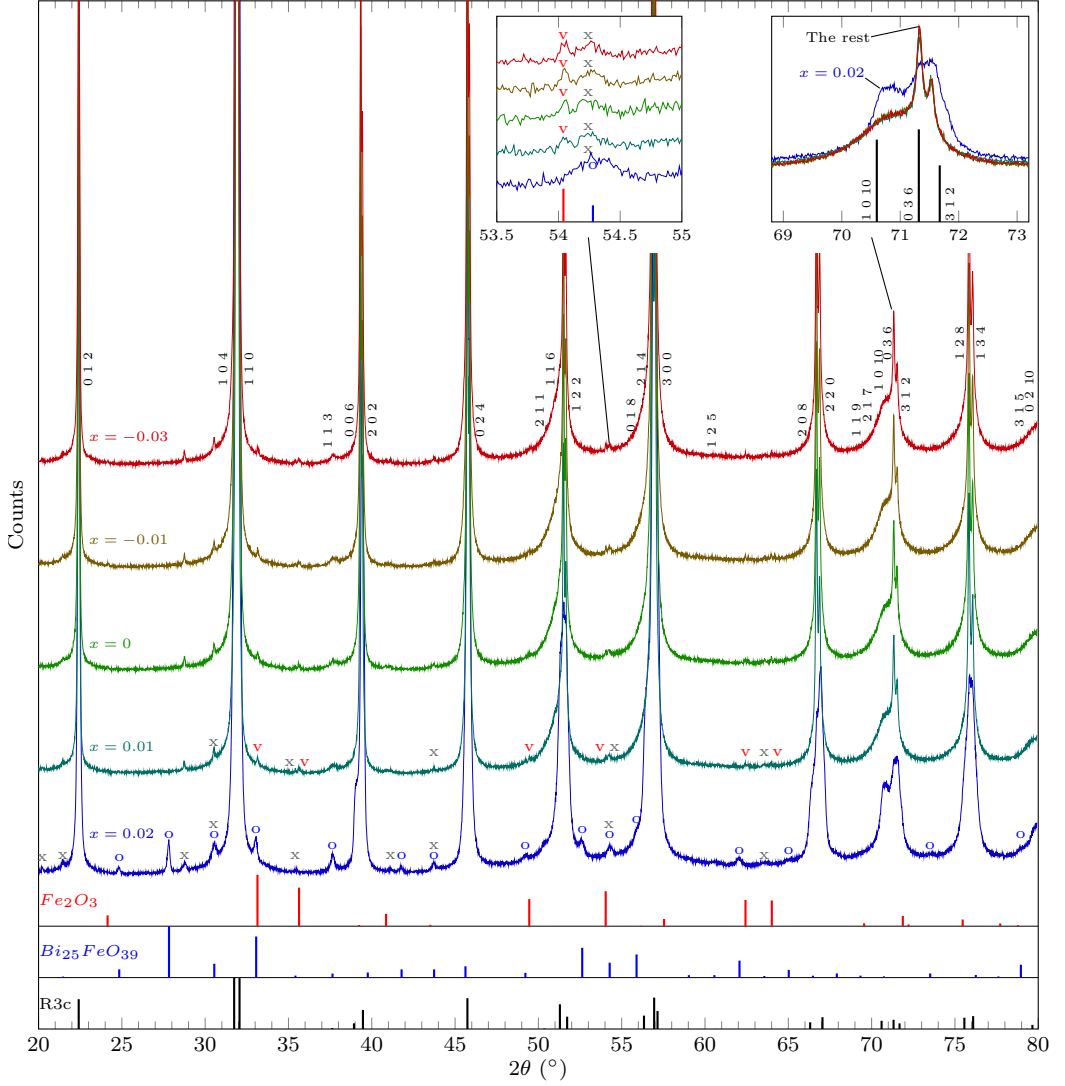


Figure 4.4.: XRD scans of all compositions. Negative and positive x correspond to A deficient and A excess, respectively. Bars labeled Fe_2O_3 (01-077-9924), $\text{Bi}_{25}\text{FeO}_{39}$ (04-008-8064) and R3c (BiFeO_3 04-009-2327) are ICDD matched structures. Secondary peaks are labeled by o ($\text{Bi}_{25}\text{FeO}_{39}$) and v (Fe_2O_3), hexagonal hkl values mark the R3c peaks, while x denotes instrument effects such as $\text{Cu}_{K\beta}$ and $W_{L\alpha}$. Insets show magnifications of selected areas, highlighting secondary peaks and peak shape. Notice that peak broadening in $x = 0.02$ is visible also in instrument effect peaks. Variable slit size yielding 6 mm illuminated sample.

4. Results

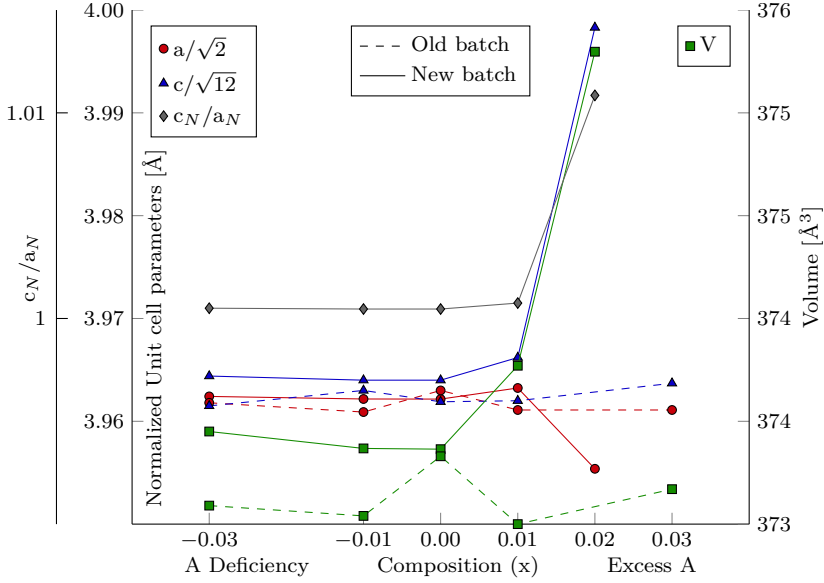


Figure 4.5.: Unit cell parameters of samples obtained through Rietveld refinement of the X-ray diffractograms in Figure 4.4 (solid lines). The dashed lines show refinement of scans conducted on samples prepared in project work.[1] The figure illustrates that $x = 0.02$ from the new batch is clearly rhombohedrally distorted, while the rest are refined close to cubic. c_N/a_N is not included for old samples because they are clearly close to cubic.

the A to B non-stoichiometry solid solution range is very narrow, or there is a problem with kinetics during sintering. The second inset in Figure 4.4 shows that the XRD peak shapes of A deficient samples are remarkably identical, supporting the notion of narrow A to B solution range. The 3% excess A sample, however, boast a significantly different peak shape, showing a definite change in crystal structure and probably vacancy concentrations.

Topas Difference in peak shapes shown in the second inset in Figure 4.4 shows the $x = 0.02$ sample to be significantly more rhombohedrally distorted, as the peak splitting is more pronounced. Compared to the other samples, the $(1010)_{hex}$ peak is both stronger and displaced toward smaller 2θ values (i.e. larger d spacings) in the 2% excess A sample. In the A deficient samples, refinement places the $(1010)_{hex}$ peak so close to $(036)_{hex}$ that they are not distinguishable from each other (i.e. very close to cubic structure). There are, however, significant peak broadening in these samples particularly on the left side of the peak, suggesting that the samples in fact do contain some distribution of c lattice parameters.

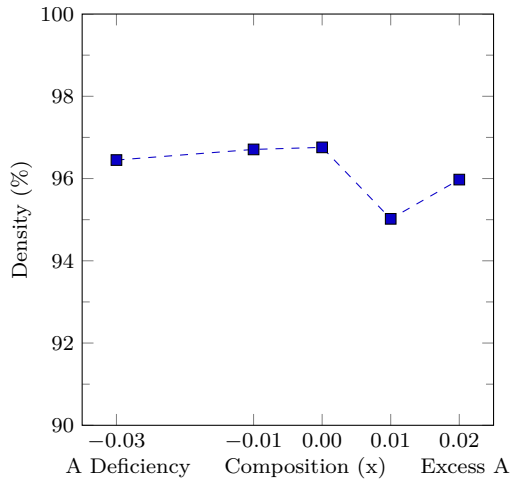


Figure 4.6.: Density of pellets measured by Archimedes' method in isopropanol. Theoretical density is calculated by interpolating the densities of pure BFO and pure BKT. Theoretical maximum has not been adjusted for excess or deficiency of A cations. Note that both of the A excess samples were sintered at 1030 °C while the other samples were sintered at 1010 °C.

Rietveld refinement of new samples (scans from Figure 4.4) and old samples is shown in Figure 4.5. The similar peak shapes and positions for A deficient samples are conveyed onto the lattice parameters. For $-0.03 < x < 0.01$ the a and c lattice parameters are within error margins the same. The rhombohedral distortion of these samples is almost non existent, as $\frac{c}{a} = 1.0005$ (normalized lattice parameters). This is also the case for all old samples, even $x = 0.03$. In the case of the new $x = 0.02$ however, this distortion measures $\frac{c}{a} = 1.011$, reflecting a stronger deviation from the cubic structure and a higher polarization. Note that the refinement is not capable of addressing hkl dependent strain, and that even though the best *mathematical* fit is close to cubic, there clearly is a distribution of c -parameters in all samples, as noted earlier.

4.2. Synthesis

Density Figure 4.6 shows that the density of all samples is high, varying from 95% to 97%. Generally, the calculated density follows x , with lower densities for A deficient samples and higher for A excess. This is in accordance with the fact that theoretical density is not adjusted for A deficiency or excess, and that A excess contains more heavy bismuth. Note however that the two excess A samples show lower densities, in accordance to the larger pore size observed in

4. Results

SEM images (Figure 4.2), and the fact that these samples are sintered at higher temperatures. The measured densities are qualitatively and quantitatively similar to that of the project work[1], indicating that the synthesis route is consistent in producing dense pellets.

Weight loss During all heat treatment stages of synthesis, the weight of the crucible and the sample were measured before and after treatment. The total weight loss during calcination was consistent at $1.55 \pm 0.05\%$ of the initial powder mass. When taking into account CO_2 from reactant K_2CO_3 and water equal to the measured hygroscopic properties of reactants, the remaining weight loss equals $0.78 \pm 0.05\%$. This corresponds to a reduction of Bi content from 0.9 to 0.89 ($Bi_{0.89}K_{0.1}Fe_{0.8}Ti_{0.2}O_{2.985}$) in the case of Bi_2O_3 evaporation or a reduction of K content from 0.1 to 0.05 ($Bi_{0.9}K_{0.05}Fe_{0.8}Ti_{0.2}O_{2.975}$) for K_2O evaporation.

These percentages are the maximum limits of possible A cation evaporation. In practice, there is also weight loss from the crucible itself, and the water and isopropanol content of the powders are only moderate estimates. The measured weight loss is very consistent however, lending credibility to the findings. Also, note that because of the much lower atomic weight of potassium compared to bismuth, the atomic amount of evaporation is 5 times higher in the case of pure K evaporation than pure Bi evaporation. If much of the weight loss in fact is A cation evaporation, it seems unlikely that the evaporation is dominated by potassium, as that would mean removing 50% of all available potassium, and reducing the total number of A cations by 5%.

The weight loss during sintering measures $0.4 \pm 0.05\%$ for pellets and $1.2 \pm 0.4\%$ for the sacrificial powder. This is neglecting all other losses, because the hygroscopic properties of BKTF-80 and crucible mass loss is unknown. In order to measure weight of pellets, any stuck sacrificial powder was scraped off with a steel spatula, which is not an accurate method. Note however, the good consistency in the results presented.

Phase purity after calcination The samples were calcined once at 820°C for 5 hours and investigated in XRD, shown in Figure 4.7.

There are some notable differences between the calcined and sintered powders. As with sintered samples, $x = -0.03$ and $x = 0.02$ contain an iron rich and bismuth rich secondary phase, respectively, but the intermediate calcined compositions contain both phases in gradually changing amounts. Note also that the Fe_2O_3 secondary phase known from the sintered samples is not present in the calcined powders, but rather another unknown phase is present. No match was found for this pattern with ICDD's 2014 database. It is, however, assumed iron rich, as the amount is gradually increasing toward A deficiency. Another notable difference is that all of the calcined powders appear to have more or less the same

perovskite peak shapes, and that the samples seem even more rhombohedrally distorted than the most distorted sintered sample. This is shown in the second inset in Figure 4.7. For the calcined powders, separation of the $(1010)_{hex}$ and $(036)_{hex}$ peaks is much more pronounced. The sintered samples, however, appear to have a distribution of $(1010)_{hex}$ peak positions. Remember that all of these labeled peaks are the same pseudocubic peak, and that these lie at the same 2θ angle for a perfect cubic perovskite.

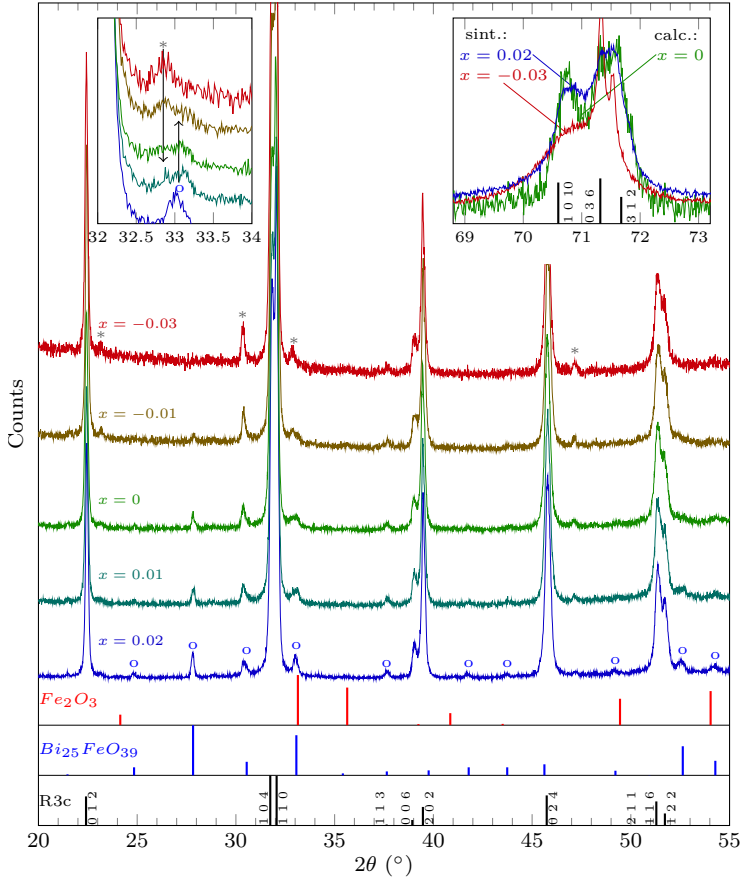


Figure 4.7.: X-ray diffractograms of calcined powders. $Bi_{25}FeO_{39}$ is present for $-0.01 < x < 0.02$ (o). Fe_2O_3 is not present in these samples, but another unknown phase (*) is assumed iron rich. The first inset show the development of the amounts of these secondary phases vs x . The second inset shows the same zoom as in Figure 4.4, and compares peak shapes of one calcined and two sintered powders. The R3c reference phase is that of pure BFO.

4. Results

Particle size after milling The calcined powders were wet milled, and the resultant powders were imaged in SEM, shown in Figure 4.8. The particles are small and the size distribution fairly narrow, as the size varies from ~ 100 to ~ 400 nm in diameter for all samples. The milling parameters are therefore considered well adjusted and successful, and diffusion lengths during sintering must have been short.

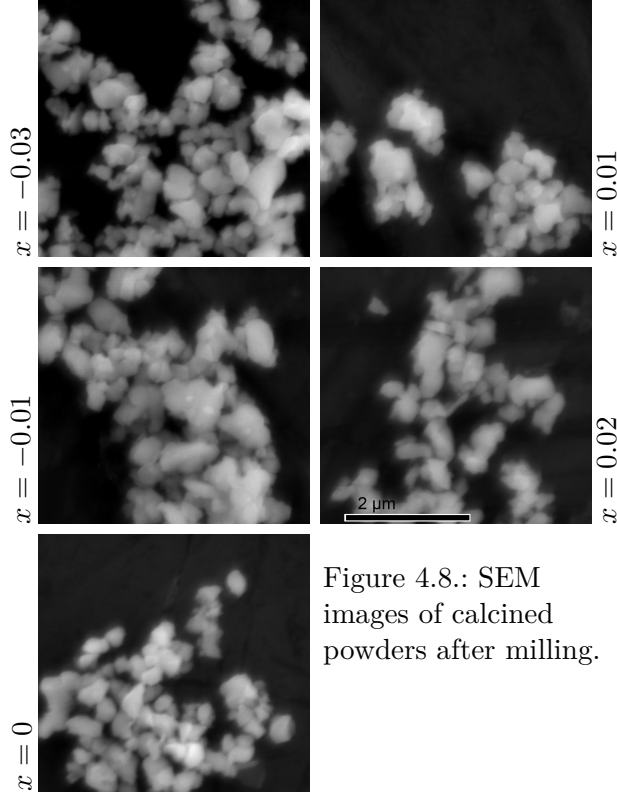


Figure 4.8.: SEM images of calcined powders after milling.

4.3. Dielectric properties

Removal of Maxwell Wagner relaxation Figure 4.9 shows dielectric properties during heating and cooling of the first heat treatment after applying electrodes to the pellets. During heating, there is a dielectric relaxation at $100 - 200^\circ\text{C}$, which (mostly) disappears during cooling. This is accredited to a Maxwell Wagner barrier effect as described by Morozov[12], and mentioned at the end of Sub Chapter 2.3.3. Notice that samples $x = 0.02$ and $x = 0$ appear to have a greater relaxation toward lower T , and that these are the samples showing the greatest decrease in conductivity during heating compared to cooling. $x = \pm 0.01$ also show a (smaller) decrease in conductivity, whilst the effect for $x = -0.03$ is too

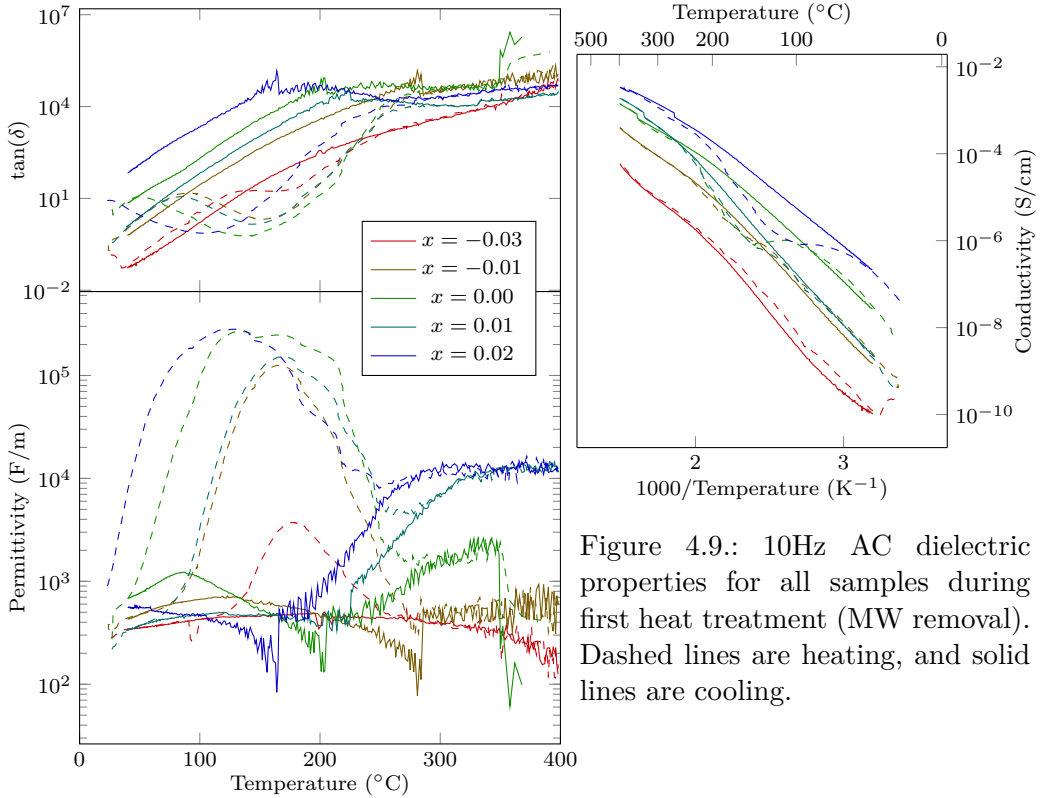


Figure 4.9.: 10Hz AC dielectric properties for all samples during first heat treatment (MW removal). Dashed lines are heating, and solid lines are cooling.

weak to appear in conductivity measurements. The relaxation is strongest for low frequencies, and 10 Hz is chosen, as lower frequencies are increasingly noisy.

From $\sim 200^\circ\text{C}$, A excess samples show a heating/cooling independent increase in permittivity that flattens out after $\sim 300^\circ\text{C}$. This effect starts at lower T for 2% excess A than for 1% excess. The stoichiometric sample also shows a similar effect, although weaker in strength. In the case of loss tangent, the effect is manifested as a small decrease in value at the same temperatures as permittivity peaks. For conductivity, the slope is decreasing toward 400°C for excess A and stoichiometric samples, and increasing for A deficient samples.

Figure A.3 is attached in the appendix, showing that the relaxation effects are stronger for low frequencies, and weaker for high frequencies.

Conductivity (High temperature) Figure 4.10 shows conductivity measurements of the stoichiometric sample for a range of frequencies. It is clear that above 200°C the conductivity is independent of frequency, and it is the direct current that is dominating, and being measured. The same pattern may be observed in the other samples (figures not supplied). Consequently, only one frequency will be presented in following conductivity

4. Results

ity plots. 10 kHz is chosen because lower frequency yields noisy permittivity data, while higher frequency yields defects in conductivity data.

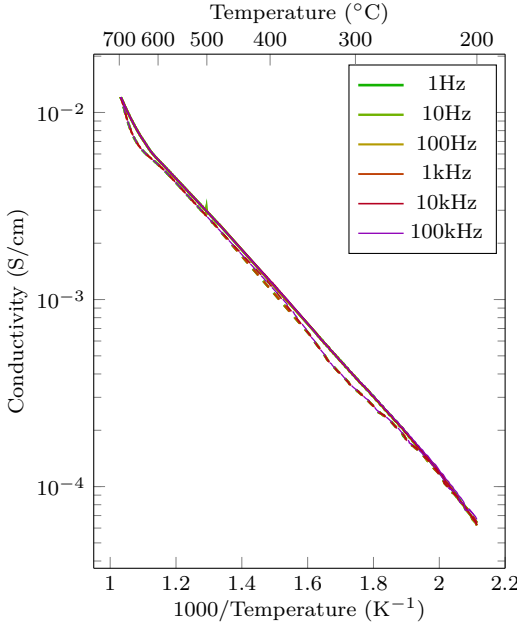


Figure 4.10.: Conductivity measurements for stoichiometric sample. Dashed: heating, solid: cooling.

generally steeper with decreasing A content, indicating difference in conductivity mechanisms and higher activation energy for A deficient samples, which are more similar to the activation energy above T_C . Stoichiometric and excess A samples have similar slopes.

Between $\sim 350 - 400^\circ\text{C}$, there is another change in slope accredited to the Neel temperature, T_N . Below this temperature all samples have similar slopes, indicating similar conduction mechanisms.

Isotherm 10Hz conductivity is shown in Figure 4.12. The decrease in conductivity is almost linear when logarithmic conductivity is plotted versus composition, with the exception of 1% A excess. The conductivity of this sample is lower than what the trend predicts.

During this work, measurements were also conducted on pellets from samples prepared in the project work[1]. These measurements are not included here, however, but rather are supplied in the Discussion Chapter when considering reproducibility of results. See Figure 5.2.

Some difference in heating/cooling curves is to be expected due to latency in temperature measurement versus the actual temperature of the sample. Generally, the temperature control/measure capabilities of the instrument is better during cooling, in addition to the fact that surface effects are less pronounced during cooling. Therefore, the cooling curves are the focus of the results (solid lines), even though heating curves are supplied for completeness (dashed lines).

Figure 4.11 shows 10 kHz high temperature conductivity for all samples. Close to 700°C all samples show a change in slope accredited to the Curie temperature¹. The slope is steeper above T_C , indicating a change toward higher activation energy in the paraelectric phase. Below T_C the slope is

¹Permittivity data below show Curie temperature peaks at $\sim 600 - 670^\circ\text{C}$, see Figure 4.13.

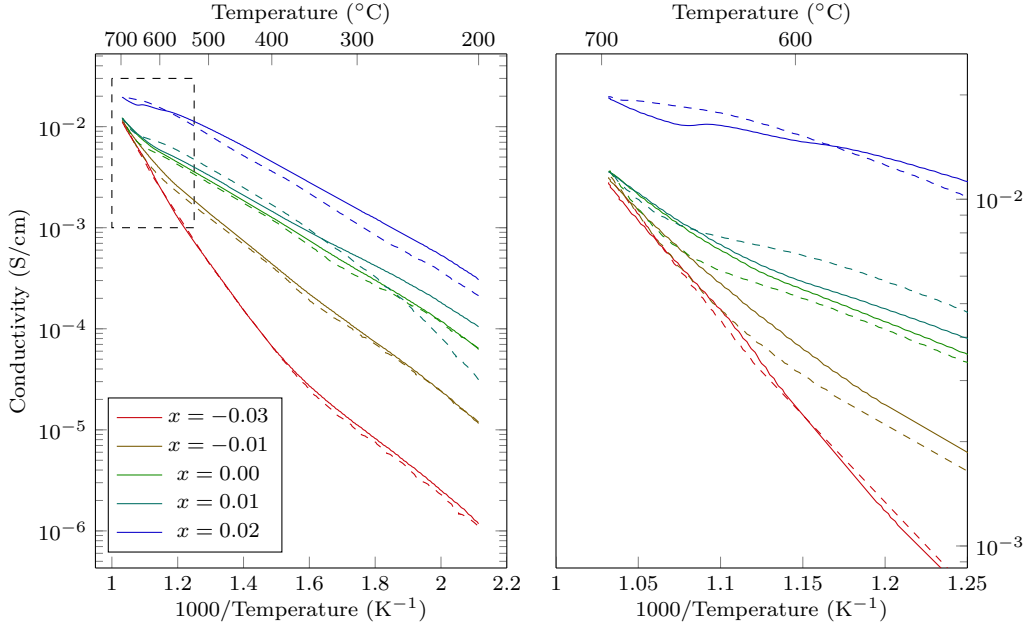


Figure 4.11.: High temperature conductivity vs temperature Arrhenius plot. Right axes shows magnification of the marked are in left axes. Dashed: heating, solid: cooling. 10 kHz AC.

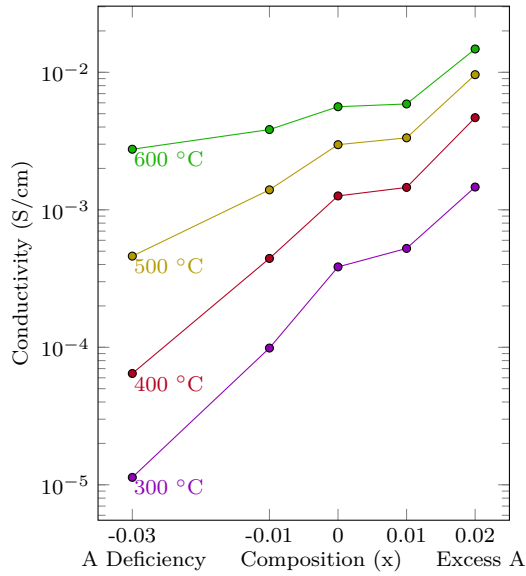


Figure 4.12.: Isotherm conductivity for all new samples during cooling. 10 kHz AC.

4. Results

Permittivity Permittivity and loss tangent for 10 kHz alternating current are shown in Figure 4.13. The Curie temperature is visible in the cooling curves as peaks between $\sim 600 - 650^\circ\text{C}$ during cooling, and closer to 700°C during heating. These peaks, and therefore also T_C , are shifted slightly toward lower temperatures for higher A content. All samples show significantly wide T_C peaks, and $x = 0.01$ even more so. The two excess A samples behave notably different from the other samples, with taller T_C peaks. For these samples there is also a significant deviation between heating and cooling curves, with tendencies of a peak at 500°C during heating which disappear during cooling. This indicates that there occur some changes in the samples during heat treatment.

Qualitatively, the $x = 0.01$ sample deviates the most from other samples, manifested by a relatively large peak close to 200°C during cooling, and a significantly wider peak around T_C . The 200°C peak appear also to some extent for stoichiometric and 2% excess A samples, but only during cooling. A deficient samples show no significant effects beside the Curie temperature peak.

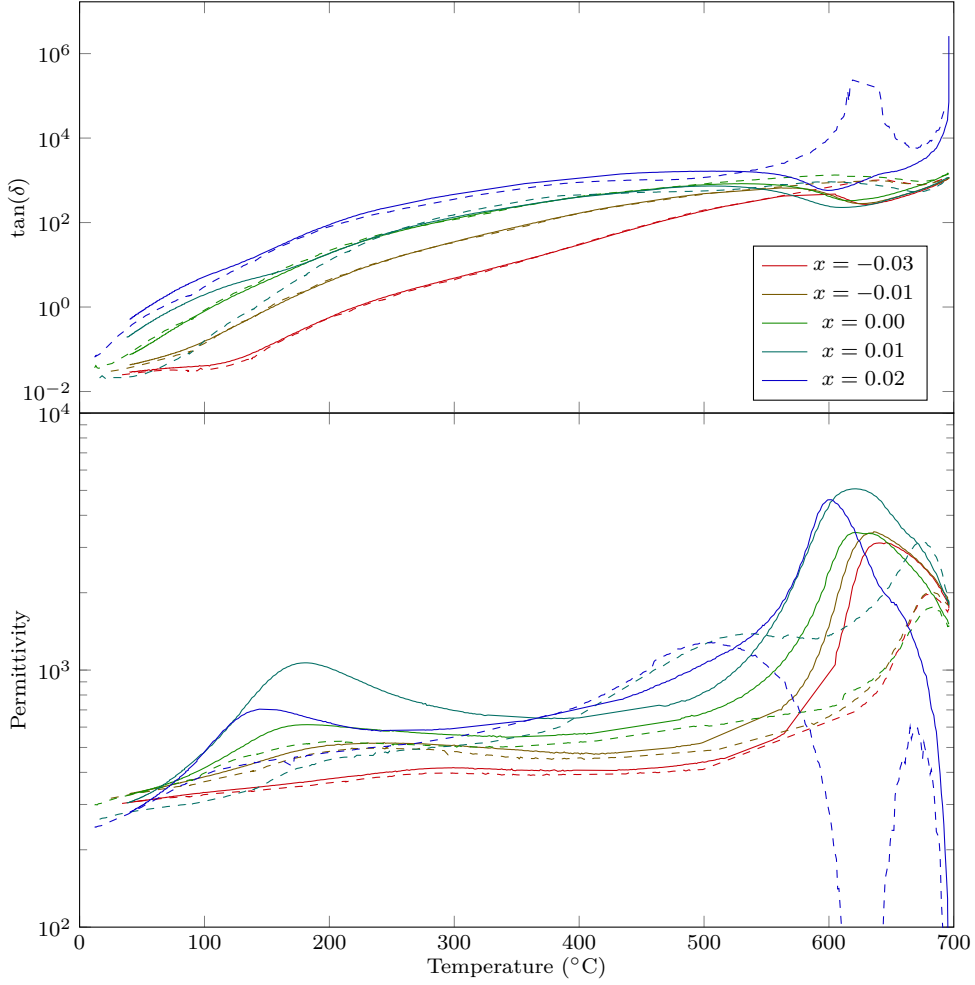


Figure 4.13.: Permittivity and loss tangent for all samples. Solid lines are cooling curves, while dashed lines are heating curves. 10kHz.

5. Discussion

5.1. Phase purity and actual stoichiometry

It was established in Chapter 4 that secondary phases only appear separately. Stoichiometric and A deficient samples contain an iron rich secondary phase, while A excess samples contain bismuth rich sillenite. Because none of the samples contains both secondary phases, it is obvious that phase impurity is not a result of the stability of the perovskite phase, as is the case in pure BFO. Inhomogeneous mixtures of reactant powders would also necessarily lead to more than one secondary phase. Rather, secondary phases must be caused by one of two reasons.

A possible explanation is that the perovskite simply is not able to accommodate the vacancy levels associated with the degree of deviation from ideal stoichiometry. One could say that the “solubility of vacancies” is low, and that the solution range of A to B unstoichiometry therefore is narrow. This, of course, corresponds to thermodynamic limits.

Another possible explanation is that (slow) kinetics is the source of secondary phases. We know from the $Bi_2O_3 - Fe_2O_3$ phase diagram (Figure 2.7) that BFO decomposes to a liquid bismuth rich phase and Fe_2O_3 as it is heated above the peritectic temperature of 960 °C. This is for pure BFO, however, and the peritectic temperature for BKTF-80 is likely considerably higher, because of the overall successful synthesis, in which the perovskite phase was obtained. If the samples were indeed sintered at too high temperatures, causing decomposition, the kinetics of diffusion into the perovskite from the time where temperature is lowered below the decomposition temperature would have defined the obtained amount of perovskite. Here, it will simply be stated that sintering temperatures did not exceed the peritectic temperature.

Remaining possible kinetic considerations for A deficient and stoichiometric samples, which show the Fe_2O_3 secondary phase, then become those connected to the equilibrium of Fe_2O_3 and perovskite during sintering. Iron oxide first melts at a temperature well above the sintering temperature, so the solid phase must have been the one present. Considering the hypothetical situation where the perovskite phase is able to solve considerably more iron (i.e. Bi vacancies) during holding, so that there are no secondary phases present, Fe_2O_3 would have been formed during cooling. In that case, slow kinetics would cause supersaturation in the perovskite phase, higher solubility, and less secondary phase than thermodynamically favorable. The opposite case, of lower vacancy concentration during

5. Discussion

holding, is not likely, due to the increased entropy at higher temperatures.

It is therefore concluded that kinetic effects may not have influenced A deficient samples toward containing more secondary phase, and that the secondary phase is thermodynamically stable.

However, A excess samples are more complicated. Sillenite melts at the eutectic temperature of 790 °C, causing A excess samples to experience liquid phase sintering. The presence of a liquid phase is supported by observation of the phase on grain boundaries and in corners between grains in SEM. Actually, in the project work, this phase was found to wet the entire grain boundaries between all perovskite grains in the 3% excess A sample.[1] Another indication of liquid phase sintering is roughly double diameter of the perovskite grains of samples exhibiting this secondary phase. The grain size difference could also originate in part from the increased sintering temperature. A combination of sources is not unlikely as liquid phase sintering is known to facilitate grain growth.

It is further seen from the phase diagram that the solubility of iron in the liquid phase rapidly increases the temperature rises. At 1000 °C, the phase diagram of Palai *et al.*[22] imply complete melting of BFO. Selbach, on the other hand, is more conservative granting only 30% Fe_2O_3 solved in the liquid phase.[28] For BKTF-80, these figures are not exactly the same, but a high concentration of iron in the liquid phase can none-the-less be expected. Simple thermodynamic considerations thus imply that the stable amount of the bismuth rich secondary phase is much greater during holding temperature, than during cooling. When the sample is cooled, the (bismuth rich) liquid phase should partition out the perovskite phase at a range of temperatures, until the eutectic temperature, where sillenite forms.

During cooling, the liquid phase will thus become more and more bismuth rich, as 1:1 Bi and Fe is removed, creating perovskite. Because the total composition always lie on the bismuth side of the perovskite phase, it is bismuth saturated (B vacancy saturated) perovskite that will be formed. Assuming again, that the vacancy concentration is larger at higher temperatures, slow kinetics should, if anything, lead to more saturated perovskite and less secondary phase. Thus, presence of the sillenite phase is also thermodynamically stable.

Another observation of these considerations is related to the chemical composition of the liquid phase. Because of the increased amount of liquid phase at higher temperatures (as a result of higher solubility of iron), some areas in the solidified samples should show signs of being liquid. This is likely to appear at the grain boundaries, considering that is where the remaining sillenite is situated. Any chemical composition of the liquid phase should thereby be conveyed onto the grain boundaries. In Figure 4.3, grain boundaries appear potassium and titanium poor, conveniently explained by a liquid phase not containing these elements. As the liquid phase solidified, BFO without (or deficient of) potassium and titanium were formed on the grain boundaries, gradually enriching the liquid phase with

bismuth, finally solidifying as $Bi_{25}FeO_{39}$ at the eutectic temperature. Thus, the grain boundaries are heavily deficient of potassium and titanium, which only to some extent is evened out by diffusion. The sillenite phase has also been identified to contain only iron in addition to bismuth oxide, as any small amount of potassium or titanium would have entered the perovskite during formation of BFO.

From the above considerations, it may with confidence be stated that the A to B stoichiometry variation feasibility, or vacancy solubility, in the perovskite phase is low. Considering Bi-rich secondary phase in $x = 0.01$, and Fe-rich secondary phase in $x = 0$, the solubility is less than 1% in both directions combined. From similar reasoning, the real 1:1 stoichiometric sample is found to be somewhere in the narrow region of $0 < x < 0.01$, not resolved by the compositions prepared during this work.

In retrospect, knowing that $x > 0.01$ possesses a secondary phase in equilibrium, the higher sintering temperatures of A excess samples was not an advantage. Using the same sintering temperatures for all samples would have yielded results of fewer unknown variables, and likely not influenced phase purity. The lack of observable secondary phase after sintering in the project work was probably a result of other effects, such as sample preparation or inhomogeneous samples.

Peak broadening The asymmetric peak broadening observed at many peaks is related to the length of the unit cell parameter c ¹. Figure 4.4 shows that the broadening happens where cubic peaks are split into peaks where one is heavily dependent on the c lattice parameter. In BFO, the c axis is elongated compared to cubic structure, causing hkl reflections of planes (close to) perpendicular to the c axis to shift toward smaller 2θ values. The actual peaks where this is observed are (116), (018) and (1010). For high quality scans of rhombohedral structures[8], these peaks are clearly separated from the a/b-perpendicular peaks, and the separation is a result of the distortion of the perovskite. In the samples prepared here, the peaks are not properly separated, but rather give a peak broadening with a distribution of c lattice parameters.

With this starting point, refinement in Topas lose much of its quantitative meaning, as a hkl dependent distribution of lattice parameters cannot be taken into account. Rather, Topas refines the diffractograms obtaining the best mathematical fit possible. For all samples but $x = 0.02$, this leads to placing the c dependent peaks at the same positions as the a/b dependent peaks, yielding a cubic structure, which is obviously not correct. In any case, the most sensible positions of c dependent peaks should be at “the edge of the peak broadening shoulders”, reflecting the most distorted parts of the samples. The $x = 0.02$ sample shows peak separation rather than a shoulder, meaning that this sample has a higher

¹Hexagonal parameters are used as default in this report.

5. Discussion

concentration of strongly distorted c parameters, and the refined c parameter of this sample does make sense although this sample probably contains some distribution of c lattice parameters as well. For all samples, the refined a -parameter should be relatively accurate, as the a dependent peaks are not broadened.

The origin of the variable lattice parameter could be ferroelectric strain. All samples were thoroughly ground using mortar and pestle, and then annealed at 700 °C which is right above the Curie temperature for 1.5 hours, in an attempt to release some of this strain. Considering the practical execution of the grinding, it is not unlikely that sufficiently small particles were not obtained. This is mainly due to two reasons, the first of which being that the samples were also intended for use in secondary phase detection. Subsequently, excessive force was avoided in fear of introducing impurities from the mortar itself. Secondly, the amount of powder used was quite large (in excess of 2 grams for each sample) and even though each sample was ground for some time, it might simply not have been enough for the amount of powder. Thus the particles annealed may have been too large to allow for strain relaxation, causing some distribution of lattice parameters to remain. Which are the real, unstrained, lattice parameters (c) is thus not credibly found, with the exception that the most A rich sample appears more rhombohedrally distorted.

This also explains the apparent stronger rhombohedral distortion of calcined powders, as the particle/crystallite size of these powders were small (Figure 4.8).

The approach used for refinement of old samples, described in Chapter 5.1, added a false intensity to the fitting at the areas of peak broadening. This allowed the rhombohedral fitting to not take the effect into account. c parameters obtained by this approach are therefore without physical meaning, as the effect defines the c parameter. On the other hand, the a parameter peaks were accurately refined, as they were not influenced by the helping phase, and because peak broadening interfering with refinement was removed.

5.2. Conductivity

Measured conductivity values did not match what was expected in the hypothesis. While a conductivity minimum in excess A samples were expected, Figure 4.12 shows that the conductivity is decreasing steadily with decreasing A content. Considering the phase purity results, it is clear that the A to B vacancy effect on conductivity will only occur in the region $0 < x < 0.01$, where the structure is not saturated on vacancies. Because all samples lie outside of this range, it is the effect of the secondary phases, and their influence on the perovskite phase, that has the main contribution to conductivity variations.

Titanium doping A deficient and stoichiometric samples show decreasing conductivity with increasing deviation from stoichiometric composition. At the same time, these samples show increasing amounts of Fe_2O_3 with little solid solution of other elements. In practice, the samples are added excess of iron and titanium (remember that the combined B cation is $(Fe_{0.8}Ti_{0.2})^{3.2+}$), and the excess titanium is not showing in any secondary phase. Excess Ti must therefore be in the perovskite phase, yielding donor doping. If the concentration of A site vacancies is the same for all samples, the amount of titanium doping is directly related to deviation from 1:1 real stoichiometry. Assuming that the nominal stoichiometry is in fact the real stoichiometry, this means 0.2% Ti doping for $x = -0.01$ and 0.6% for $x = -0.03$. When taking into consideration bismuth and potassium evaporation, the values will be up to 0.2 % higher (corresponding to 1% A cation evaporation). In any case, these values of Ti doping are within the solvable range of Ti in BKTF-80 found in unpublished work by Wefring[34]. Wefring also proves that Ti-doping effectively reduces conductivity, in accordance with p-type conduction, although not to the extent measured here. He found that high temperature conductivity of BKTF-80 is decreased by $\sim 10^1$ by doping with 1% Ti_{Fe} . Similarly, the conductivity increased by $\sim 10^{0.5}$ for 1% Fe_{Ti} (iron doping, or titanium removal).[34] Xu *et al.* have also found that donor doping of $\sim 4\%$ Sn reduces the conductivity of BFO by more than one order of magnitude.[29]

Whether all excess titanium enters the perovskite at the cost of iron is supported by titanium solubility in the perovskite. Generally, based on tolerance factor, titanium is expected to be more stable in the perovskite phase than iron (see Chapter 2.3.1). At temperatures $\sim 200 - 400^\circ\text{C}$, the Arrhenius slopes (Figure 4.11) are very similar, indicating equal activation energies/band gaps, which again indicates that the same conductivity mechanism is prevailing. If this is the case, the difference in absolute conductivity is a result of concentration of charge carriers, as is the effect of donor doping.

Another effect of titanium doping is diluting of iron on B site. The activation energy of polaron hopping is dependent on availability of sites of holes. When titanium is introduced to the B site, available iron sites are removed. In the present case, the stoichiometric concentration of iron on B site is 80%. At 0.6% titanium doping, this concentration is reduced by $\frac{0.6\%}{80} = 0.75\%$, which is too low to likely have a noticeable effect on conductivity.

Potassium doping Similar to that of titanium doping for A deficient samples, A excess samples may be potassium doped to some extent. Considering an A rich secondary phase without potassium, this should lead to acceptor doping, as excess K is in the perovskite instead of in the secondary phase. The argumentation is the same as for titanium doping, but the effect will be increased p-type conductivity for excess A, rather than decreased conductivity for A deficiency. While the

5. Discussion

off-valence of titanium is 1+ compared to iron, and potassium is 2– compared to bismuth, titanium constitute 20% of the B cations, and potassium constitute 10% of the A cations, yielding the same “magnitude of doping”.

Bi₂O₃ ion conduction Oxygen ion conduction in Bi_2O_3 as high as 10^0 S/cm at 700 °C was reported in the 1980’s by Harwig *et al.*[43] This phase is closely related to the secondary phase observed in A excess samples, and conductivity in this phase may partly explain the higher conductivity of 2% excess A compared to the other samples. The phase is shown to be positioned at the grain boundaries, and in the project work[1], it was observed to create a network along perovskite grains, completely wetting the grain boundaries. It is not unlikely that this phase drastically increase the overall conductivity of the sample through grain boundary conduction.

Another aspect of this phase is that it may facilitate the reach of oxygen to the perovskite phase and therefore the oxidation of iron. High levels of oxygen ion conduction along the grain boundaries could mean significantly shorter diffusion lengths for oxygen, and lead to a higher degree of iron oxidation on the perovskite phase. Presence of this phase may also shift the oxygen partial pressure/ Fe^{4+} equilibrium, influencing the stable concentration of holes.

Fe-O-Fe angle Conductivity variations may also be a result of variations in crystal structure and orbital overlaps. Increased overlap of orbitals correspond to a narrower band gap (i.e. shorter polaron hopping distance), and would therefore give lower activation energies, and higher conductivity. Increased overlap may result from straighter Fe-O-Fe angles[16] or a compressed unit cell. Unit cell parameters obtained in this work is not showing much (systematic) variation, however, and little is therefore known about the angle development.

One exception is that $-0.03 < x < 0.01$ appear more cubic, and Selbach found that the conductivity of BFO decrease slightly over the paraelectric phase transition, from ferroelectric $Pbnm$ to paraelectric $Pm\bar{3}m$. [28] This is none-the-less unlikely to explain the observed conductivity, as this effect is weak.

Other effects Doping and Bi_2O_3 grain boundary conduction alone are not likely to explain the whole picture, as the difference in conductivity from $x = -0.03$ to $x = 0.02$, of about two decades, is greater than what is reported for similar conditions. Therefore some other, currently unknown effects are possibly present.

One aspect is the validity of the p-type conduction assumption. Unpublished work by Wefring have shown that even moderately reducing atmospheres during heat treatment of BKTF-80 produce n-type conductivity. That is, the stability of oxidized iron is not as great as previously expected, and the influence of oxidizing conditions may not be that important.

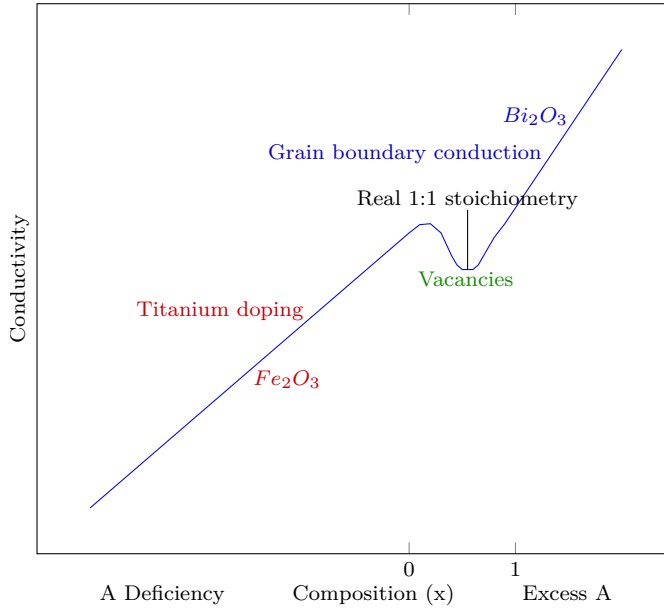


Figure 5.1.: Proposed qualitative conductivity. The labels indicate which effect has the greatest influence on conductivity at different regions of the graph.

Another possible influence is reactions between the electrode and the sample. Bismuth forms an eutectic alloy, Bi_2Pt , with platina at 270 °C, and even more phases exist at higher temperatures.[16] Platina electrodes were used in the measurements, separated from the sample by a gold layer, however. It is possible that interactions with the electrodes may also influence total conductivity.

Other aspects are not yet identified, but probably play a significant role.

Oxygen vacancies Although it has been stated that secondary phases dominate the conductivity variations, the hypothesis may qualitatively still be correct. Within the solubility range of the material, a vacancy dependent variation could exist. This would yield a drop in conductivity between $x = 0$ and $x = 0.01$, as sketched in Figure 5.1. The drop however, is negligible in comparison to secondary phase effects. In the figure, observed conductivity from Figure 4.12 is taken as a starting point, adding the expected effect of vacancy concentration, as described in the hypothesis. The secondary phases possibly responsible for conductivity, or lack thereof, is marked on appropriate parts of the graph.

5.3. Old batch compared to new batch

Phase purity For both old and new samples, iron oxide is detected in A deficient samples. Similarly, sillenite was detected for $x = 0.03$ in the old samples, and for $x = 0.01, 0.02$ in the new samples. Figure A.4 is adapted from the project work[1], and shows both similar secondary phases and similar micro structure. The reproducibility of micro structure and obtained secondary phases is thus good, lending credibility to the findings of the current work.

The peak shapes of A deficient samples are also very similar between batches, as shown by similar refined lattice parameters in Figure 4.5. In total, phase purity, peak shapes, densities, micro structure, and vacancy concentration appear to be reproduced well between batches.

Conductivity The conductivity results of the two batches, however, are not as similar. Figure 5.2 shows isotherm conductivity for old samples measured in the current work, deviating significantly from the conductivity of the new batch. This shows that reproducibility is poor, and even small variations influence conductivity greatly. These variations may be impurities introduced during synthesis, impurities on the surface of the pellet, inhomogeneities, and related issues.

Generally, the new batch appears significantly more credible. This is demonstrated by the conductivity in Figure 5.2, which shows a significant temperature dependence. $x = 0.03$ decrease in conductivity (relative to the other samples) as temperature is decreased, while $x = 0.01$ show opposite behavior, indicating the presence of several uncontrolled effects. In the new batch, however, a temperature independent conductivity variation is shown. In addition to this, permittivity measurements of old samples (Figure A.5), show more peaks, indicating several additions to dielectric properties.

Some conductivity differences may be explained by the preparation of the samples. New samples were polished and cleaned in ultrasonic bath, while the old samples only were rinsed. Because of this, old samples may have been dirtier at the surface, possibly leading to uncontrolled surface effects at the gold electrodes. The dirt may for example have been silicon carbide from the grinding step resting in the open pores on the surface.

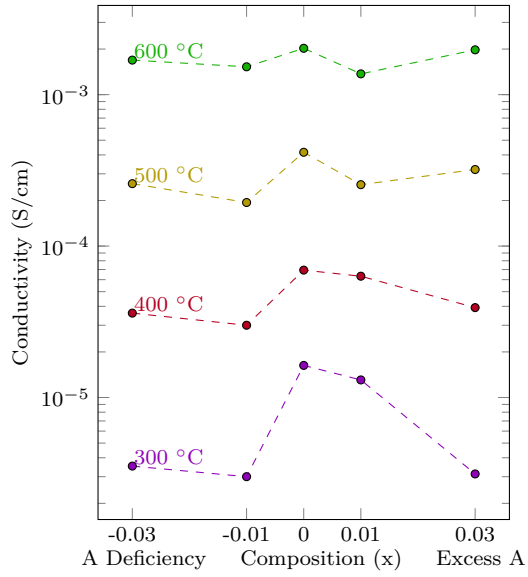


Figure 5.2.: Isotherm conductivity measurements of old samples (measured in the current work). 10 kHz AC.

6. Concluding remarks and further work

Phase purity, micro structure, and secondary phases obtained are reproducible, and show that the evaporation of A cations are between 0 and 1at%. The solubility of A to B stoichiometry variation is low, producing sillenite ($Bi_{25}FeO_{39}$) when more than 1% A is added in excess, and iron oxide for stoichiometric and A deficient samples. Care must be taken designing the optimal A to B stoichiometry in order to prepare phase pure samples, due to the narrow solubility range. With the current synthesis route, 0.5% excess A may be a good starting point.

Because excess titanium or potassium do not create secondary phases when added in excess, but rather introduce doping, only varying bismuth and iron content (as opposed to the combined A/B cations) should yield better A to B stoichiometry (vacancy concentration) results. Because of the limited vacancy concentration limits, however, the resultant effect on oxygen vacancies and holes will be small. For conductivity reasons, focus should rather be on secondary phases, thermal history, and dopants.

In order to better determine the source of conductivity, heat treatment in both reducing and oxidizing atmospheres should be conducted. Any deviations between the samples will reveal different conduction mechanisms (i.e. n-type versus p-type), and can therefore also shed light on the exact influence of impurities. Atmospheric history would also help in identifying a possible oxygen ion conduction in the 2% A excess sample. This is important because the conductivity mechanism must be understood in order to successfully tune it.

Topas refinement showed varying quality of the results, possibly related to strain and too large particle size. In order to gain better knowledge of the crystal structure of the samples, more thorough grinding and subsequent annealing before scanning in XRD may yield better results.

Bibliography

- [1] Mads Christensen. “Investigation of the effect of A-B stoichiometry variation on conductivity in $0.2\text{Bi}_{0.5}\text{K}_{0.5}\text{TiO}_3 - 0.8\text{BiFeO}_3$ ”. Project work. NTNU, Trondheim, 2013.
- [2] Juergen Roedel et al. “Perspective on the development of lead-free piezoceramics”. In: *Journal of the American Ceramic Society* 92.6 (2009), pp. 1153–1177. DOI: 10.1111/j.1551-2916.2009.03061.x.
- [3] Gene H. Haertling. “Ferroelectric ceramics: history and technology”. In: *Journal of the American Ceramic Society* 82.4 (1999), pp. 797–818. DOI: 10.1111/j.1151-2916.1999.tb01840.x.
- [4] Elena Aksel and L. Jones Jacob. “Advances in lead-free piezoelectric materials for sensors and actuators”. In: *Sensors (Basel)* 10.3 (2010), pp. 1935–54. URL: <http://www.mdpi.com/1424-8220/10/3/1935/pdf>.
- [5] J. F. Carvalho and A. C. Hernandez. “Growth and optical characterization of cerium and lead-doped $\text{Bi}_{12}\text{TiO}_{20}$ sillenite single crystals”. In: *Crystal Research and Technology* 40.9 (2005), pp. 847–851. DOI: 10.1002/crat.200410444.
- [6] Wei-Tin Chen et al. “Robust Antiferromagnetism and Structural Disorder in $\text{BixCa}_{1-x}\text{FeO}_3$ Perovskites”. In: *Chemistry of Materials* 21.10 (2009), pp. 2085–2093. DOI: 10.1021/cm8031048.
- [7] J. M. Kim et al. “Piezoelectric and dielectric properties of lead-free $(1-x)(\text{Bi}_{0.5}\text{K}_{0.5})\text{TiO}_3-x\text{BiFeO}_3$ ceramics”. In: *Ferroelectrics* 404 (2010), pp. 88–92. DOI: 10.1080/00150193.2010.482448.
- [8] Maxim I. Morozov, Mari-Ann Einarsrud, and Tor Grande. “Polarization and strain response in $\text{Bi}_{0.5}\text{K}_{0.5}\text{TiO}_3\text{-BiFeO}_3$ ceramics”. In: *Applied Physics Letters* 101.25 (2012), pp. 252904/1–252904/4. DOI: 10.1063/1.4772588.
- [9] Maxim I. Morozov et al. “Lead-Free Relaxor-Like $0.75\text{Bi}_{0.5}\text{K}_{0.5}\text{TiO}_3 - 0.25\text{BiFeO}_3$ Ceramics with Large Electric Field-Induced Strain”. In: *Ferroelectrics Letters* 439.1 (2012), pp. 88–94. DOI: 10.1080/00150193.2012.741946.
- [10] Maxim I. Morozov et al. “Influence of the A/B nonstoichiometry, composition modifiers, and preparation methods on properties of Li- and Ta-modified $(\text{K,Na})\text{NbO}_3$ ceramics”. In: *Journal of Applied Physics* 112.11 (2012), pp. 114107/1–114107/9. DOI: 10.1063/1.4768211.

- [11] Maxim I. Morozov, Mari-Ann Einarsrud, and Tor Grande. “Control of conductivity and electric field-induced strain in bulk Bi_{0.5}K_{0.5}TiO₃ - BiFeO₃ ceramics”. 2014.
- [12] Maxim I. Morozov, Mari-Ann Einarsrud, and Tor Grande. “Atmosphere controlled conductivity and Maxwell-Wagner relaxation in Bi_{0.5}K_{0.5}TiO₃—BiFeO₃ ceramics”. In: *Journal of Applied Physics* 115.4 (2014), p. 044104. DOI: 10.1063/1.4863798.
- [13] Michael Naderer et al. “The influence of Ti-nonstoichiometry in Bi_{0.5}Na_{0.5}TiO₃”. In: *Journal of the European Ceramic Society* 34.3 (2014), pp. 663–667. DOI: 10.1016/j.jeurceramsoc.2013.10.010.
- [14] Tadej Rojac, Marija Kosec, and Dragan Damjanovic. “Large electric-field induced strain in BiFeO₃ ceramics”. In: *Journal of the American Ceramic Society* 94.12 (2011), pp. 4108–4111. DOI: 10.1111/j.1551-2916.2011.04861.x.
- [15] T. T. Carvalho and P. B. Tavares. “Synthesis and thermodynamic stability of multiferroic BiFeO₃”. In: *Materials Letters* 62.24 (2008), pp. 3984–3986. DOI: 10.1016/j.matlet.2008.05.051.
- [16] Gustau Catalan and James F. Scott. “Physics and Applications of Bismuth Ferrite”. In: *Adv. Mater. (Weinheim, Ger.)* 21.24 (2009), pp. 2463–2485. DOI: 10.1002/adma.200802849.
- [17] Valdirlei Fernandes Freitas et al. “Structural phase relations in perovskite-structured BiFeO₃-based multiferroic compounds”. In: *Journal of Advanced Ceramics* 2.2 (2013), pp. 103–111. DOI: 10.1007/s40145-013-0052-2.
- [18] Toshimitsu Ito et al. “Growth of Highly Insulating Bulk Single Crystals of Multiferroic BiFeO₃ and Their Inherent Internal Strains in the Domain-Switching Process”. In: *Crystal Growth & Design* 11.11 (2011), pp. 5139–5143. DOI: 10.1021/cg201068m.
- [19] M. Mahesh Kumar et al. “Ferroelectricity in a pure BiFeO₃ ceramic”. In: *Applied Physics Letters* 76.19 (2000), pp. 2764–2766. DOI: 10.1063/1.126468.
- [20] A. R. Makhdoom et al. “Association of microstructure and electric heterogeneity in BiFeO₃”. In: *Materials Chemistry and Physics* 143.1 (2013), pp. 256–262. DOI: 10.1016/j.matchemphys.2013.08.061.
- [21] Nahum Maso and Anthony R. West. “Electrical Properties of Ca-Doped BiFeO₃ Ceramics: From p-Type Semiconduction to Oxide-Ion Conduction”. In: *Chemistry of Materials* 24.11 (2012), pp. 2127–2132. DOI: 10.1021/cm300683e.

- [22] R. Palai et al. “ phase and - metal-insulator transition in multiferroic BiFeO₃”. In: *Physical Review B* 77.1 (2008). DOI: 10.1103/PhysRevB.77.014110.
- [23] Jason Schiemer et al. “Detailed Phase Analysis and Crystal Structure Investigation of a Bi_{1-x}CaxFeO_{3-x/2} Perovskite-Related Solid Solution Phase and Selected Property Measurements Thereof”. In: *Chemistry of Materials* 21.18 (2009), pp. 4223–4232. DOI: 10.1021/cm901757h.
- [24] Sverre M. Selbach et al. “Size-Dependent Properties of Multiferroic BiFeO₃ Nanoparticles”. In: *Chemistry of Materials* 19.26 (2007), pp. 6478–6484. DOI: 10.1021/cm071827w.
- [25] Sverre M. Selbach et al. “Synthesis of BiFeO₃ by wet chemical methods”. In: *Journal of the American Ceramic Society* 90.11 (2007), pp. 3430–3434. DOI: DOI10.1111/j.1551-2916.2007.01937.x.
- [26] Sverre M. Selbach et al. “The ferroic phase transitions of BiFeO₃”. In: *Adv. Mater. (Weinheim, Ger.)* 20.19 (2008), pp. 3692–3696. DOI: 10.1002/adma.200800218.
- [27] Sverre Magnus Selbach, Mari-Ann Einarsrud, and Tor Grande. “On the Thermodynamic Stability of BiFeO₃”. In: *Chemistry of Materials* 21.1 (2009), pp. 169–173. DOI: 10.1021/cm802607p.
- [28] Sverre Magnus Selbach. “Structure, stability and phase transitions of multiferroic BiFeO₃”. Doctoral thesis. NTNU, Trondheim, 2009.
- [29] Q. Xu et al. “The role of Bi vacancies in the electrical conduction of BiFeO₃: a first-principles approach”. In: *Dalton Trans* (2014). DOI: 10.1039/c4dt00468j.
- [30] Takuro Ikeda and Tatsuya Okan. “Piezoelectric ceramics of lead zirconate-titanate modified by bismuth ferrite”. In: *Japanese Journal of Applied Physics* 2 (1963), pp. 63–4.
- [31] S. A. Fedulov et al. “High temperature x-ray and thermographic studies of bismuth ferrite”. In: *Kristallografiya* 6 (1961), pp. 795–6.
- [32] J. Wang et al. “Epitaxial BiFeO₃ multiferroic thin-film heterostructures”. In: *Science (Washington, DC, U. S.)* 299.5613 (2003), pp. 1719–1722. DOI: 10.1126/science.1080615.
- [33] Hiroki Matsuo et al. “Structural and piezoelectric properties of high-density (Bi_{0.5}K_{0.5})TiO₃-BiFeO₃ ceramics”. In: *Journal of Applied Physics* 108.10 (2010), pp. 104103/1–104103/6. DOI: 10.1063/1.3506717.
- [34] Espen Tjønneland Wefring. “Unpublished work”. NTNU - Trondheim, 2013.
- [35] Wikipedia. *Space Group*. Web Page. URL: http://en.wikipedia.org/wiki/Space_group.

- [36] Wikipedia. *Frenkel defect*. Web Page. URL: http://en.wikipedia.org/wiki/Frenkel_defect.
- [37] Wikipedia. *Schottky defect*. Web Page. URL: http://en.wikipedia.org/wiki/Schottky_defect.
- [38] K. Momma and F. Izumi. “VESTA 3 for three-dimensional visualization of crystal, volumetric and morphology data”. In: *Journal of Applied Crystallography* 44 (2011), pp. 1272–1276. DOI: 10.1107/S0021889811038970.
- [39] A. V. Pushkarev, N. M. Olekhovich, and Yu V. Radyush. “Dielectric properties of perovskite ceramics of $(1-x)\text{BiFeO}_3 - x(\text{KBi})_{1/2}\text{TiO}_3$ ($0.40 < x < 0.85$) solid solutions from impedance spectroscopy data”. In: *Phys. Solid State* 53.3 (2011), pp. 522–526. DOI: 10.1134/s1063783411030267.
- [40] Chamaiporn Wicheanrat, Artid Laowanidwatana, and Theerachai Bongkarn. “Influences of Excess Bi_2O_3 and K_2CO_3 on Crystal Structure, Microstructure and Dielectric Properties of Bismuth Potassium Titanate Ceramics”. In: *Integr. Ferroelectr.* 149.1 (2013), pp. 9–17. DOI: 10.1080/10584587.2013.852891.
- [41] M. V. Raymond and D. M. Smyth. “Nonstoichiometry, defects, and charge transport in PZT”. In: *NATO ASI Series, Series E Applied Physics* 284. Science and Technology of Electroceramic Thin Films (1995), pp. 315–25.
- [42] Fengkuo Zhao et al. “Effect of nonstoichiometric Pb content on the properties of PZT ceramics”. In: *Adv. Mater. Res. (Durnten-Zurich, Switz.)* 415-417.Pt. 3, Advanced Materials (2012), pp. 1883–1887. DOI: 10.4028/www.scientific.net/AMR.415-417.1883.
- [43] H. A. Harwig and A. G. Gerards. “Electrical properties of the , , and phases of bismuth sesquioxide”. In: *Journal of Solid State Chemistry* 26.3 (1978), pp. 265–274. DOI: [http://dx.doi.org/10.1016/0022-4596\(78\)90161-5](http://dx.doi.org/10.1016/0022-4596(78)90161-5).

A. Additional figures

A.1. Rietveld refinement

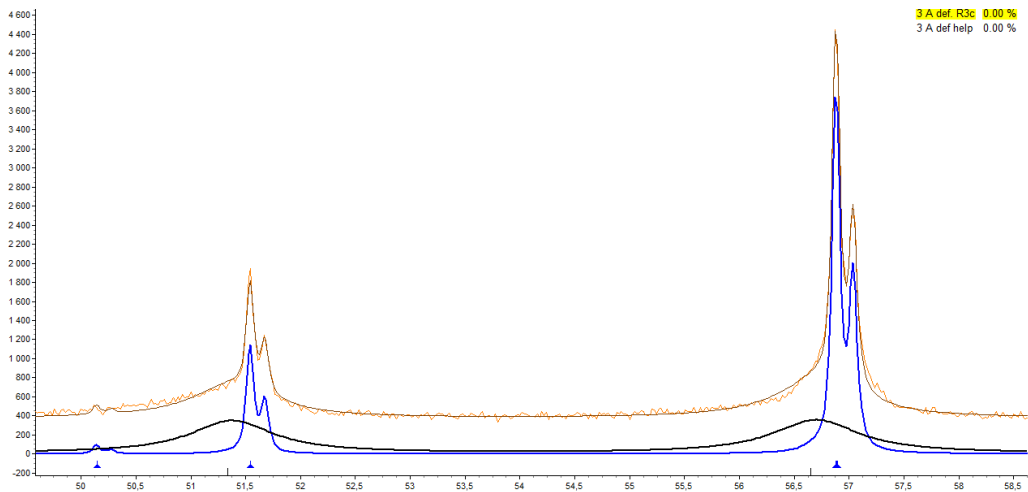


Figure A.1.: Fitting in Topas using a “helping” phase supplying the black line. The blue line shows the fitting of the rhombohedral R3c phase. The orange line is the collected data, and the thin line is the resultant total fit. Stoichiometric sample.

A. Additional figures

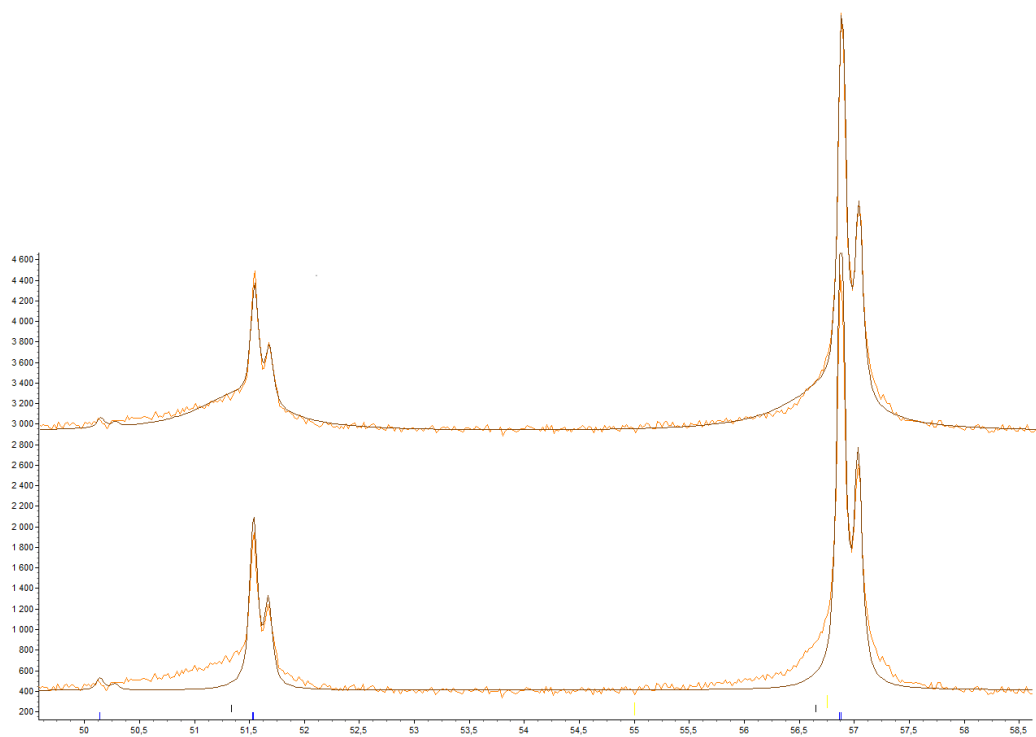


Figure A.2.: Topas fitting result with (top) and without (bottom) helping phase. Stoichiometric sample.

A.2. Dielectric measurements

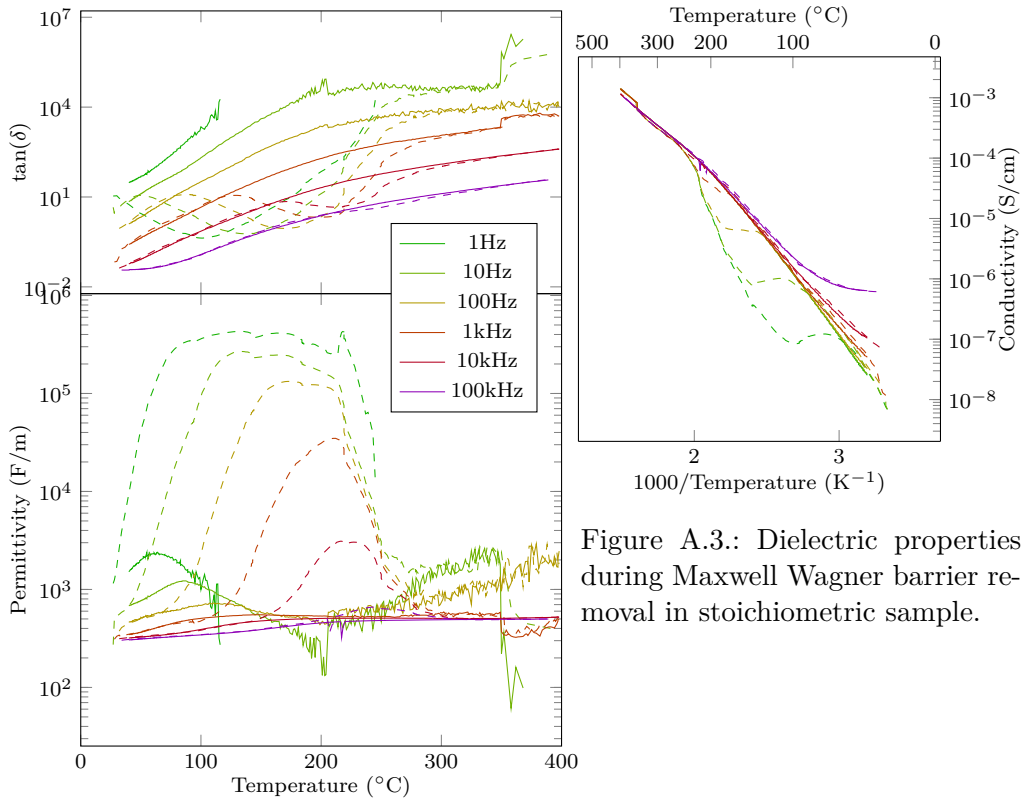
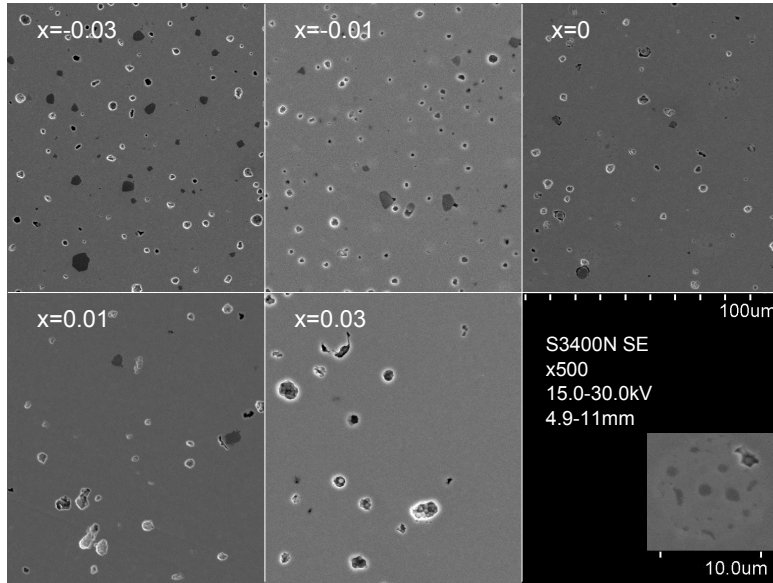
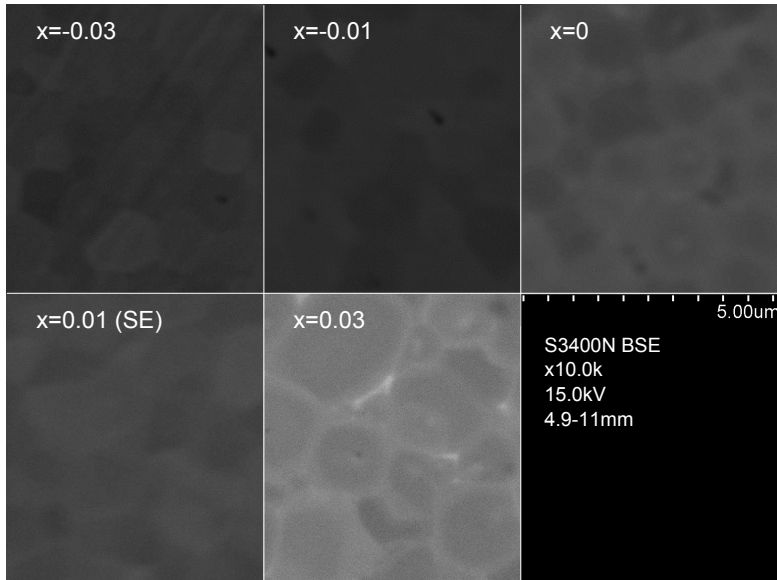


Figure A.3.: Dielectric properties during Maxwell Wagner barrier removal in stoichiometric sample.

A.3. Results of old batch



(a) Overview. Inset: Agglomerate in $x = 0$.



(b) Grain size

Figure A.4.: SEM images adapted from the project work.[1] An iron rich secondary phase is visible for $-0.03 < x < 0.01$, and $x = 0.03$ show the sillenite phase. These were confirmed in EDS (figure not supplied).

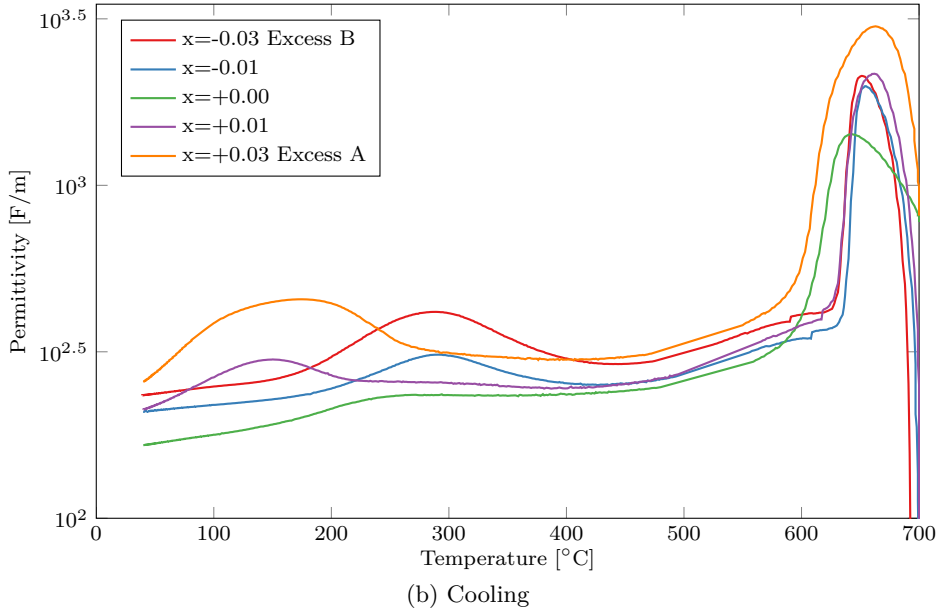
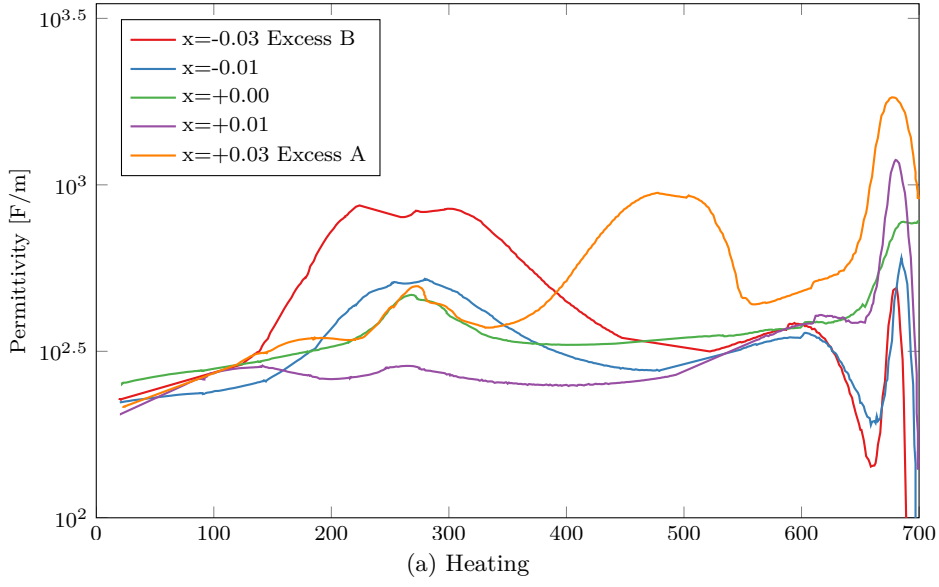


Figure A.5.: 10 kHz permittivity of old samples adapted from[1].